NEUROSCIENCE

Invasion of phagocytic Galectin 3 expressing macrophages in the diabetic brain disrupts vascular repair

Eslam M. F. Mehina[1], Stephanie Taylor[1], Roobina Boghozian[1], Emily White[1], Sun Eui Choi[1], Manjinder S. Cheema[1], Jakob Korbelin[2], Craig E. Brown[1,3]*

The cellular events that dictate the repair of damaged vessels in the brain, especially in those with vascular risk factors such as diabetes, is poorly understood. Here, we dissected the role of resident microglia and infiltrative macrophages in determining the repair of ruptured cerebral microvessels. Using in vivo time-lapse imaging, gene expression analysis, and immunohistochemistry, we identified a unique population of phagocytic Galectin 3 (Gal3) expressing macrophages, distinct from resident microglia, which infiltrated and aggregated at the site of injury in diabetic mice and were associated with the elimination of microvessels. Depletion of these infiltrative macrophages in diabetic mice attenuated phagocytic activity and prevented the loss of blood vessels after injury. These findings highlight a previously unknown role for infiltrative Gal3 expressing macrophages in promoting vessel elimination after brain injury and provide impetus for future studies to determine whether depleting these cells can facilitate vascular repair in at risk populations.

INTRODUCTION

Diabetes mellitus (DM) is a highly prevalent and debilitating metabolic disorder that is commonly associated with profound vascular pathology including stroke, retinopathy, and cerebral microbleeds (CMBs). CMBs are spontaneous ruptures in cortical capillaries and penetrating arterioles that often go unnoticed as they do not present with overt clinical symptoms. However, these ruptures trigger the release of toxic substances within blood plasma, such as iron and fibrinogen, which can disrupt nearby neuronal circuitry (*1*–*3*). Since these insults can occur spontaneously and accumulate over a lifetime, the burden of CMBs has been correlated with cognitive decline and the onset or progression of dementia (*4*, *5*). Given that patients with type 1 diabetes (DB) are at increased risk for CMBs and vascular disease (*6*, *7*) and that insulin treatment is ineffective in fully mitigating this pathology (*8*), it is imperative to identify previously unknown strategies to help repair vessels in the diabetic brain.

To repair damaged or ruptured blood vessels, the brain must recruit local and peripheral immune cells. Microglia are a specialized type of yolk sac–derived macrophage that resides in the central nervous system (*9*, *10*). Within minutes of vascular injury and lasting for several days, microglia enwrap their processes around damaged microvessels and stem the extravasation of toxic blood plasma to restore the cohesion of the blood brain barrier (BBB) (*11*). Local microglia comprise the predominant immune cell type recruited to damaged microvessels, but a small number of invasive macrophages, normally excluded by the specialized structure of the BBB under homeostatic conditions, also respond to these insults. For example, recent in vivo imaging has shown that a few circulating macrophages are recruited to CMB injury sites within 24 to 48 hours and can linger there for several days (*12*, *13*). Both protective and degenerative roles have been ascribed to microglia and infiltrative macrophages in healthy and diseased states, reflecting their ability to exhibit both pro- and anti-inflammatory roles (*14*). For example, infiltrative macrophages could help repair damaged vessels and stitch them back together (*15*, *16*), or they could attack and phagocytize injured vessels (*17*, *18*). Similarly, while microglia likely play a beneficial role in repair, at least initially (*8*, *11*, *19*, *20*), over time, they may prolong brain injury or promote neuronal and vascular degeneration (*21*–*24*). Since both resident microglia and blood-borne macrophages are recruited to injury sites, what role each cell type may play in dictating the fate of damaged microvessels (i.e., whether vessels recanalize and persist or disintegrate) remains an important, but unresolved, question. Furthermore, how a chronic inflammatory disease such as type 1 DB, which also increases the risk of vascular injury, influences the recruitment of microglia/macrophages and subsequent vascular repair is unknown.

Our initial experiments in healthy mice revealed that microvessels ruptured in vivo with a femtosecond laser invariably recanalized and persisted throughout our 14-day imaging period. However, when the exact same injury was induced in mice with type 1 DB, a subset of injured vessels was eventually eliminated. We took advantage of these differences in vessel outcomes to probe the cellular mechanisms that dictate microvascular repair, particularly in the context of a chronic inflammatory vascular disease such as DB. Analysis of gene expression patterns after CMB and immunohistochemical identification of subpopulations of cells recruited to the injury site revealed the presence of macrophages expressing Galectin 3 (Gal3) in the diabetic brain. These cells were also highly enriched with markers of phagocytosis and infiltrated sites where vessels were eliminated. Our findings compliment previous single-cell transcriptomic studies that found that up-regulated expression of *Lgals3* by immune cells in disease or aging was associated with amoeboid-shaped phagocytic cells (*25*, *26*). Eradicating most peripheral phagocytic leukocytes with systemic clodronate liposome (CLR) treatment prevented the aggregation of Gal3 expressing macrophages around CMBs and improved microvascular repair in diabetic mice.

[1]Division of Medical Sciences, University of Victoria, Victoria, BC, Canada. [2]Department of Oncology, Hematology and Bone Marrow Transplantation, University Medical Center Hamburg-Eppendorf, Hamburg, Germany. [3]Department of Psychiatry, University of British Columbia, Vancouver, BC, Canada.
*Corresponding author. Email: brownc@uvic.ca

Our data highlight the complexity of cellular responses to cerebrovascular insults and identify a previously unknown role for Gal3 expressing macrophages in regulating the elimination of microvessels in the brain.

RESULTS

DB is associated with increased phagocytic activity and abnormal elimination of microvessels after microbleed

Building on previous findings showing that type 1 DB perturbed acute microglial responses to CMBs (≤1 hour after induction) and impaired closure of the BBB after injury (*8*), we tested whether DB could also affect repair of microvessels over days and ultimately compromise their functional reintegration into the cerebral circulation. To address this question, we performed longitudinal two-photon imaging through a cranial window in young adult male mice from three experimental groups: (i) nondiabetic (NDB) mice; (ii) mice with uncontrolled DB, induced via multiple, low-dose streptozotocin (STZ) injections; and (iii) diabetic mice with blood glucose levels managed via chronic, slow-release insulin implants (DB + INS; Fig. 1A). As expected, STZ treatment led to a significant increase in blood glucose levels in the diabetic group that remained elevated for 4 weeks (Fig. 1B). Blood glucose levels in insulin-treated mice were normalized by week 2 [nine of nine mice; see inset in Fig. 1B; two-way analysis of variance (ANOVA) for blood glucose from weeks 1 to 4, time: $F_{4,98} = 5.34$, $P < 0.001$; treatment: $F_{2,98} = 62.94$, $P < 0.0001$; interaction: $F_{6,88} = 6.18$, $P < 0.0001$]. To induce vascular damage, we ruptured a fluorescently labeled microvessel with brief (~6 s), high-power femtosecond laser scanning, targeting microvessels within 50 to 100 μm below the pial surface in the somatosensory cortex. Successful induction of CMBs was confirmed in all cases by the presence of an extravascular fluorescent plume and cessation of blood flow within targeted microvessels. Using heterozygous CX3CR1$^{GFP/+}$ mice to visualize microglia/macrophages in vivo, we were able to characterize the evolving immune cell response to injury and determine whether ruptured capillaries would recanalize and persist over 14 days (i.e., defined as a "repaired" vessel) or be eliminated. Consistent with previous imaging work (*12*, *27*), green fluorescent protein (GFP)–expressing microglia/macrophages formed a plaque around the damaged microvessel that was evident for 1 to 7 days after CMB and subsided within 14 days in 72% of cases (79 of 109 vessels targeted; Fig. 1, C to E). However, in healthy NDB mice, all targeted microvessels ($n = 43$ vessels) regained blood flow and were maintained over the 2-week imaging period (Fig. 1, C, F, and G). By contrast, 20% of microvessels targeted in diabetic mice were permanently eliminated (9 of 45 vessels eliminated; Fig. 1, D, F, and G). Insulin treatment did not prevent this microvascular loss, and 18% of targeted microvessels were eliminated following CMB (6 of 34 vessels eliminated; Fig. 1, E to G). This difference in vessel outcomes was significant regardless of whether they were analyzed with each CMB representing a single observation (Fig. 1F) or whether multiple CMBs within the same animal (separated by at least 250 μm) were averaged together (Fig. 1G). Examination of time-lapse data revealed that microvessels were eliminated by 3 days after CMB induction, with some instances of vessel loss evident within 1 day following injury (Fig. 1H). To ensure that these group differences in microvascular elimination rates were not attributed to variations in the characteristics of targeted microvessels, we confirmed that there were no significant differences between experimental groups with respect to (i) blood flow velocity before CMB induction, (ii) vessel diameter, and (iii) length (fig. S1, A to C). Although average blood flow velocity did not differ significantly between groups, we noted a trend for lower values in both untreated and insulin-treated diabetic groups (mean = 0.54 ± 0.04 and 0.58 ± 0.05 mm/s, respectively) relative to healthy NDB mice (mean = 0.68 ± 0.04 mm/s; fig. S1A).

To assess differences in the phagocytic response to CMBs in diabetic and NDB mice, we analyzed the autofluorescent signal from lipofuscin (lipid particles contained in lysosomal compartments of phagocytic cells), which can be visualized in vivo using two-photon microscopy. To validate our lipofuscin analysis, we first examined colocalization of lipofuscin with the classical phagolysosomal marker CD68 (fig. S2A). Our data showed that, while CD68 tends to have a greater area of expression than lipofuscin (fig. S2B), all lipofuscin signal was colocalized with CD68 immunostaining (fig. S2C). Having confirmed a relationship between the lipofuscin signal and CD68$^+$ lysosomes, we assessed the lipofuscin content within cells responding to CMBs in NDB and diabetic mice (Fig. 2A). Our analysis revealed a significant increase in lipofuscin 1 day after induction of CMB [Fig. 2B; two-way mixed-effects model ANOVA, main effect of time: $F_{4,297} = 21.26$, $P < 0.0001$; Tukey's multiple comparisons test, day 0 (D0) versus D1: $P < 0.0001$]. Notably, lipofuscin signal in diabetic mice was significantly greater after CMB at all imaging time points than that observed in the NDB group (Fig. 2B; two-way mixed-effects model ANOVA, main effect of treatment group: $F_{1,85} = 12.91$, $P = 0.0005$). As an internal control to confirm that these changes in lipofuscin were specific to cells responding to the CMB, we assessed lipofuscin in GFP-expressing microglia/macrophages distant (>40 μm) to the bleed and found only a slight increase in signal over time (Fig. 2B; two-way mixed-effects model ANOVA, main effect of treatment group: $F_{1,85} = 1.449$, $P = 0.2321$; main effect of time: $F_{4,297} = 2.869$, $P = 0.0387$; Tukey's multiple comparisons test, D0 versus D3: $P = 0.0104$ and D0 versus D7: $P = 0.0072$). Expectedly, lipofuscin signal within GFP-expressing cells was significantly higher when the ensheathed microvessels were eliminated rather than repaired (Fig. 2C; unpaired Student's t test, $P < 0.0001$). These data support the notion that microglia/macrophages specifically responding to CMBs are highly phagocytic, especially under diabetic conditions.

To further understand why vessel outcomes were affected by DB, we characterized the morphometric features of the CX3CR1 GFP–expressing cellular aggregate around the CMB at each imaging time point, both with respect to its two-dimensional area and the extent to which it covered the length of the vessel (Fig. 2D). The area of GFP expression peaked at the lesion site in the first day and progressively decreased over 14 days, a phenomenon that did not differ significantly between groups (Fig. 2E; two-way mixed-effects model ANOVA, main effect of time: $F_{1.754,171.4} = 18.07$, $P < 0.0001$; main effect of treatment: $F_{2,114} = 0.3255$, $P = 0.7228$). Similarly, there were no group differences in GFP-expressing cell coverage of targeted vessels (Fig. 2F; two-way mixed-effects model ANOVA, main effect of treatment: $F_{2,109} = 0.06862$, $P = 0.9337$). This response peaked 1 day after CMB in all groups (NDB: 53.461 ± 3.579%, $n = 41$; DB: 56.490 ± 3.698%, $n = 44$; DB + INS: 58.647 ± 4.694%, $n = 23$) and comparably declined over the 2-week imaging period (Fig. 2F; main effect of time: $F_{2.313,216.7} = 139.6$, $P < 0.0001$). Since there were no significant group differences in area of GFP expression or vessel coverage to explain vessel outcomes, we parsed the data further to determine whether microglial response characteristics

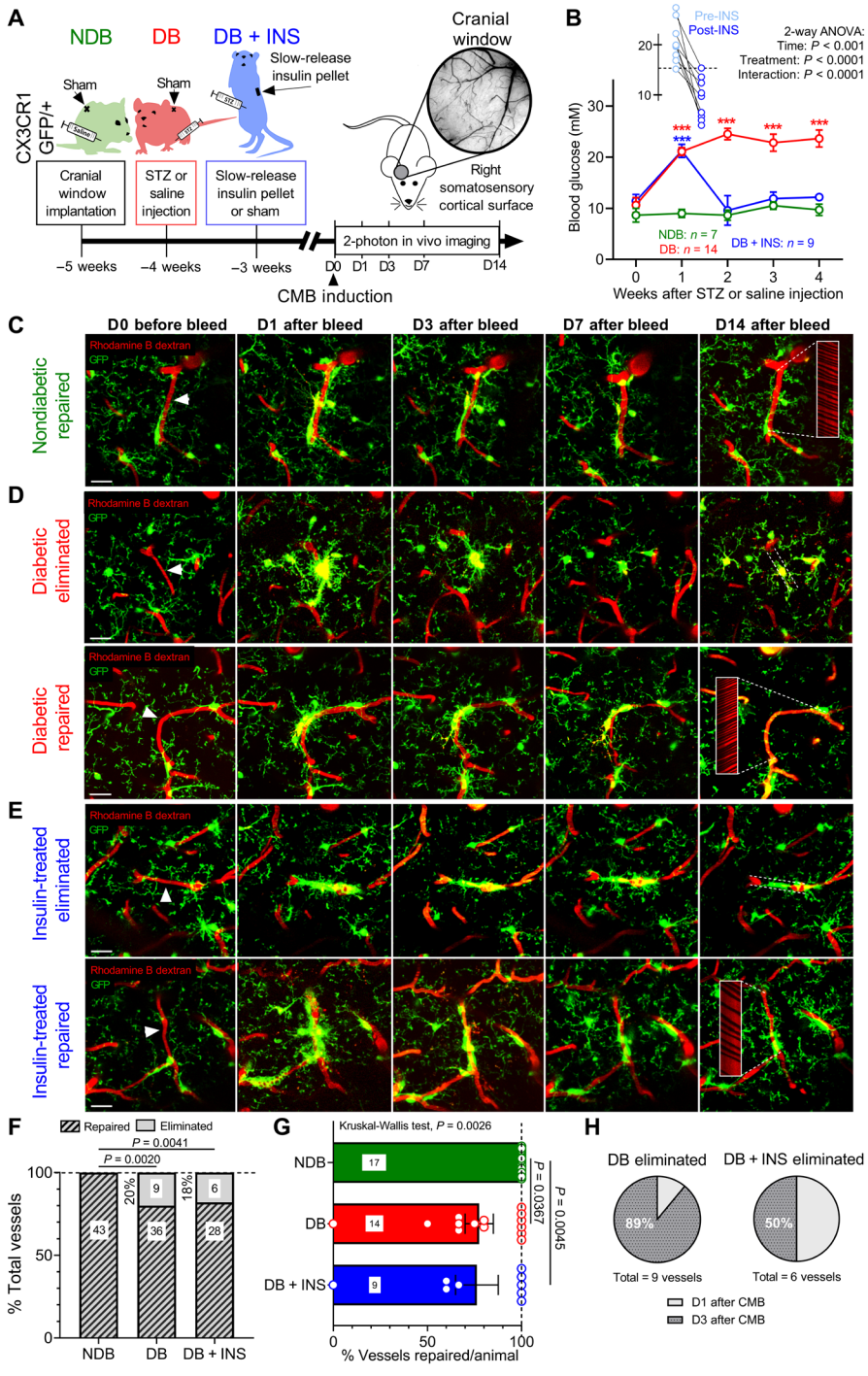

Fig. 1. Time-lapse in vivo imaging of GFP-expressing microglia/macrophage responses to CMB reveals the abnormal elimination of microvessels in diabetic mice. (**A**) Graphical representation of experimental timeline and treatment groups. (**B**) Average blood glucose readings for experimental groups measured at weekly intervals. Inset highlights the normalization of blood glucose values in individual diabetic mice receiving insulin treatment. (**C** to **E**) In vivo *z*-projection images illustrate the evolving response of GFP-expressing microglia/macrophages following induction of cortical CMB (site of CMB induction indicated by white arrowhead). Patent blood vessels were visualized with intravenous injection of rhodamine B dextran, and line scans (insets) show the presence of blood flow (line scans with streaks indicate a flowing vessel). Note that, in some cases, ablated microvessels were repaired and preserved, whereas, particularly in the diabetic group, others were eliminated. Scale bars, 20 μm. (**F**) Graph summarizing the percentage of microvessels that were repaired or eliminated following induction of CMB in NDB ($n = 43$ bleeds from 17 mice), diabetic ($n = 45$ bleeds from 14 mice), and insulin-treated diabetic mice ($n = 34$ bleeds from nine mice). (**G**) Percentage of microvessels repaired per animal. (**H**) Pie charts showing the proportion of vessels eliminated at 1 or 3 days after CMB induction in diabetic and insulin-treated groups. Statistics based on two-way ANOVA with post hoc Tukey's multiple comparisons tests (B), chi-squared analysis (F), and nonparametric Kruskal-Wallis test with post hoc Dunn's multiple comparisons test (G). Error bars represent means ± SEM.

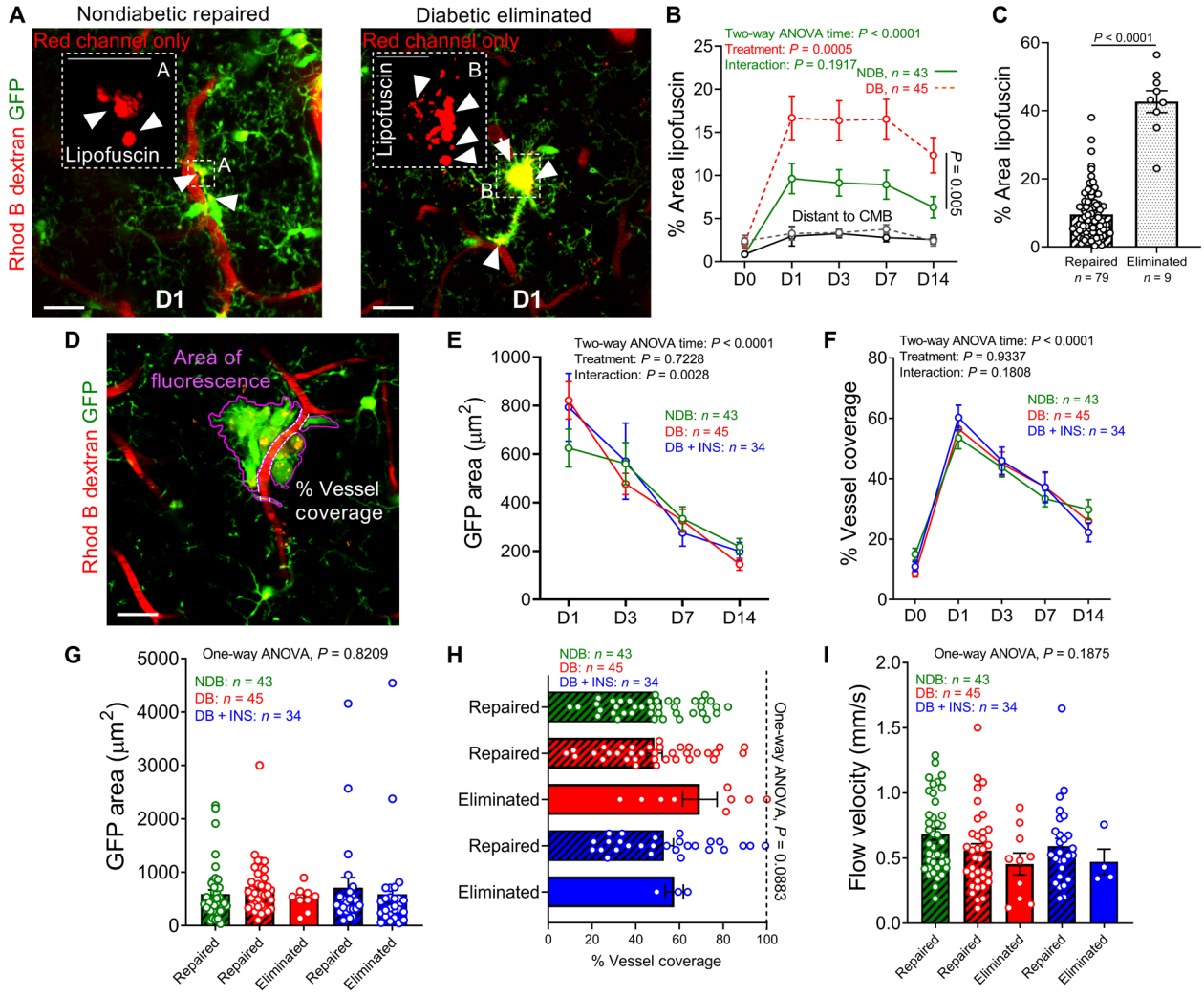

Fig. 2. DB is associated with increased phagocytic activity but not greater accumulation or coverage of GFP-expressing cells at bleed sites. (**A**) Representative two-photon images showing rhodamine B dextran labeling of plasma within blood vessels and lipofuscin autofluorescent signal outside of vessels localized within CX3CR1 GFP–expressing microglia/macrophages 1 day after CMB. Unlike rhodamine B, autofluorescent lipofuscin puncta appear as yellow deposits in green/red images (white arrowheads) due to their broad spectral emission characteristics in both channels. Scale bars, 20 μm. Insets show thresholded and binarized images of lipofuscin particles. Scale bars, 10 μm. (**B**) Graph summarizing the percent area of lipofuscin autofluorescence within microglia/macrophage aggregates at the site of the CMB over time (colored lines) or within microglia/macrophages distant from the lesion site (>40 μm). (**C**) Average percentage area of lipofuscin in microvessels that were repaired versus those that were eliminated. (**D**) Representative two-photon image showing how GFP fluorescence area (purple outline) and vessel coverage (white dashed lines) were assessed. Scale bar, 20 μm. Graphs show the area of GFP fluorescence (**E**) and the percentage of vessel coverage (**F**) at bleed sites in each experimental group over time. (**G**) Area of GFP fluorescence following CMB (based on average of D1 and D3) in vessels that were repaired or eliminated in each group. (**H**) Average percentage of vessel coverage (based on average of D1 and D3) in vessels that were repaired or eliminated in each group. (**I**) Average blood flow velocities at D0 (before CMB), in targeted microvessels that eventually repaired or were eliminated. Statistics were based on two-way mixed-effects model ANOVAs (B, E, and F), unpaired Student's *t* test (C), and one-way ANOVA with post hoc Tukey's multiple comparison tests as appropriate (G to I). Error bars represent means ± SEM.

varied depending on whether a microvessel was repaired or eliminated. To this end, we found that neither the total area of GFP fluorescence (Fig. 2G) nor the percentage of vessel coverage (Fig. 2H), examined as an average of D1 and D3 values, were associated with vessel repair or elimination in any groups (one-way ANOVA, $P = 0.8209$ and one-way ANOVA, $P = 0.0883$, respectively). Furthermore, since it is conceivable that slow flowing vessels may be more susceptible to elimination than fast flowing ones, we examined blood flow velocity (measured before CMB) in microvessels that were eventually repaired or eliminated. Our analysis revealed no relationship between baseline blood flow and the eventual fate of a damaged microvessel (Fig. 2I; one-way ANOVA, $P = 0.1875$). To rule out the possibility that our GFP expression analysis may be influenced by prelesion group differences in microglia expression, we performed immunolabeling for transmembrane protein 119 (TMEM119), a reliable marker of resident microglia (*28*), and confirmed that there were no significant differences in microglial density between groups (fig. S3, A and B; one-way ANOVA, $P = 0.6012$), which replicates previous work from our laboratory (*8*). Furthermore, since the GFP expression analysis could be influenced by group differences in the number of cells responding to the CMB, we labeled and quantified all nucleated cells with Hoechst 33342 and did not find any group

differences in the average number of cells present at the lesion site (fig. S3, C and D; unpaired Student's *t* test, $P = 0.1712$). Lastly, since previous studies suggested that microglia in the hippocampus of diabetic mice may appear more amoeboid (*29*, *30*), we analyzed soma cross-sectional area and total process length per microglia from two-photon image stacks collected before the induction of microbleeds. Our analysis did not reveal any significant differences between experimental groups in terms of average soma volume or total process length per microglia (fig. S3E; one-way ANOVA, $F_{2,47} = 0.13$, $P = 0.87$; and one-way ANOVA, $F_{2,47} = 0.16$, $P = 0.85$, respectively). Collectively, these results show that GFP-expressing cells aggregate around CMBs and that type 1 DB, even when treated with insulin, is associated with greater vessel loss after CMB. Moreover, differing vessel fates could not be predicted by morphometric analyses of GFP-expressing cell responses or prelesion differences in microvessel diameter, length, or blood flow velocity.

Delayed appearance of GFP-expressing macrophages at the lesion site in microglia-depleted mice is associated with microvessel elimination

Since CX3CR1 GFP is expressed in resident microglia and meningeal/perivascular macrophages, as well as circulating monocyte-derived macrophages, we sought to disentangle the relative contributions of these different cells to vessel repair after CMB. To this end, NDB and diabetic mice were administered chow containing the colony-stimulating factor-1 receptor (CSF1R) antagonist PLX5622 [1200 parts per million (ppm)] for 3 weeks before induction of CMBs. Consistent with previous work (*31*), PLX5622 diet depleted 87.37 ± 1.61% ($n = 19$) and 84.78 ± 1.33% ($n = 32$) of microglia in NDB and diabetic mice, respectively, within 3 weeks (Fig. 3, A and B; two-way mixed-effects model ANOVA, main effect of PLX5622 over time: $F_{3,78} = 971.5$, $P < 0.0001$; main effect of DB: $F_{1,49} = 0.6801$, $P = 0.4135$). Given that some circulating blood cells can express CSF1R, we quantified monocytes, neutrophils, lymphocytes, and red blood cells (RBCs) from blood smears and found that they were not significantly affected by PLX5622 treatment (Fig. 3, C to E; neutrophils: one-way ANOVA, $P = 0.7288$; monocytes: one-way ANOVA, $P = 0.5622$; lymphocytes: one-way ANOVA, $P = 0.9886$). Furthermore, none of these white blood cells or RBCs were significantly affected by DB (Fig. 3, D and E). Although PLX5622 treatment depleted most resident TMEM119-expressing microglia, time-lapse in vivo imaging revealed that, despite inducing CMBs at a distance from any remaining microglia, we still observed GFP-labeled cells at the lesion site (at 1 day after CMB) in 91% of cases (Fig. 3F). Notably, in some cases, we captured a stationary GFP-labeled cell within the vascular lumen next to the damaged microvessel (see arrowhead in Fig. 3G), which could represent a macrophage before transmigration into the brain parenchyma. This observation is consistent with recent reports showing that microglial depletion with PLX5622 facilitates invasion of infiltrating macrophages (*32*, *33*). We therefore parsed the data relating to microvessel outcomes according to the presence or absence of GFP-expressing cells at the lesion site, irrespective of the diabetic condition. Our analysis showed that when GFP-expressing cells invaded the lesion site, 20% of microvessels were eliminated (Fig. 3, F and H), similar to what we reported in diabetic mice (see Fig. 1E). When GFP-expressing cells did not appear at the CMB, microvessels were preserved in all cases (Fig. 3, F and H). Next, we analyzed vessel outcomes according to different treatment groups and found that 27% of microvessels were eliminated in PLX5622-treated diabetic mice, which was 7% higher compared to untreated diabetic mice (Fig. 3I). However, microglial depletion in NDB mice led to an unusual elimination of microvessels after CMB, which was never observed in NDB controls that did not receive PLX5622 (Fig. 3I; 18% versus 0% elimination, respectively). These findings were also evident if the data were analyzed using the mean percentage of vessels repaired per animal for all groups (Fig. 3J). In summary, our results suggest that the invasion of CMB lesions by GFP-expressing cells, likely of peripheral origin given that >84% of resident microglia were eliminated, is associated with increased risk of vessel elimination.

Gal3 is up-regulated in the injured diabetic brain and expressed in phagocytic macrophages associated with microvessel elimination

Next, we considered the possibility that bleed sites could be infiltrated by macrophages, such as those residing on the brain's surface or from the circulation. Meningeal and perivascular macrophages populate the pial surface and exist along large penetrating vessels, respectively (fig. S4A) and could conceivably migrate to the lesion site (*34*). We first probed their presence at CMB sites in postmortem tissue using the validated meningeal/perivascular macrophage marker CD206 (*34*). We determined that, while PLX5622 treatment significantly reduced the number of CD206-expressing cells along the meninges and penetrating blood vessels (fig. S4B; unpaired Student's *t* test, NDB versus PLX5622: $P = 0.0332$; unpaired Student's *t* test, DB versus PLX5622: $P = 0.0086$), some cells still persisted and, therefore, could have potentially infiltrated CMBs. However, analysis of CD206 expression at the site of CMBs in postmortem tissue from NDB and diabetic mice did not reveal any $CD206^+$ cells (fig. S4, C and D). Therefore, CD206-expressing meningeal and perivascular macrophages do not appear to comprise the population of cells that are recruited to CMB sites.

On the basis of our finding that a PLX5622-resistant cell could appear at bleed sites within 24 hours, in conjunction with an elegant previously unknown study showing that PLX5622-resistant microglia/macrophages express Gal3 (*35*), we directed our attention toward these particular cells. In accordance with this recent report, we confirmed that, while most resident microglia expressing TMEM119 were depleted with PLX5622, Gal3 expressing cells in the brain were generally spared (fig. S5, A and B; unpaired Student's *t* test, $TMEM119^+$ control versus PLX5622: $P < 0.0001$; unpaired Student's *t* test, $Gal3^+$ control versus PLX5622: $P = 0.6486$) as were $Gal3^+$ macrophages in the spleen. Next, we quantified the expression of phagocytic- and disease-related genes in the cortex of diabetic and NDB mice 3 days after induction of CMBs. Specifically, we investigated key genes involved in orchestrating macrophage phagocytosis (*Lgals3*, *Cd68*, *Trem2*, *Cd206*, *Mertk*, and *Axl*) and the development of inflammatory diabetic pathology, including nephropathy (*TGF-β1*, *TGF-βR1*, and *Apoe*) (*36*). Since *TMEM119* can be down-regulated in microglia during inflammation or injury (*37*), we also assessed its expression. Our analysis revealed that CMBs led to a significant up-regulation of cortical *Lgals3* and *CD68* gene expression, particularly in diabetic mice (Fig. 4A); *Trem2* expression was increased, but not significantly. To identify the phenotype of individual cells at bleed sites, we induced CMBs in diabetic and NDB mice in vivo (Fig. 4B) and then, 3 days after CMB induction, confirmed which microvessels were repaired or eliminated. We then extracted, sectioned, and immunolabeled the brains and used the relative

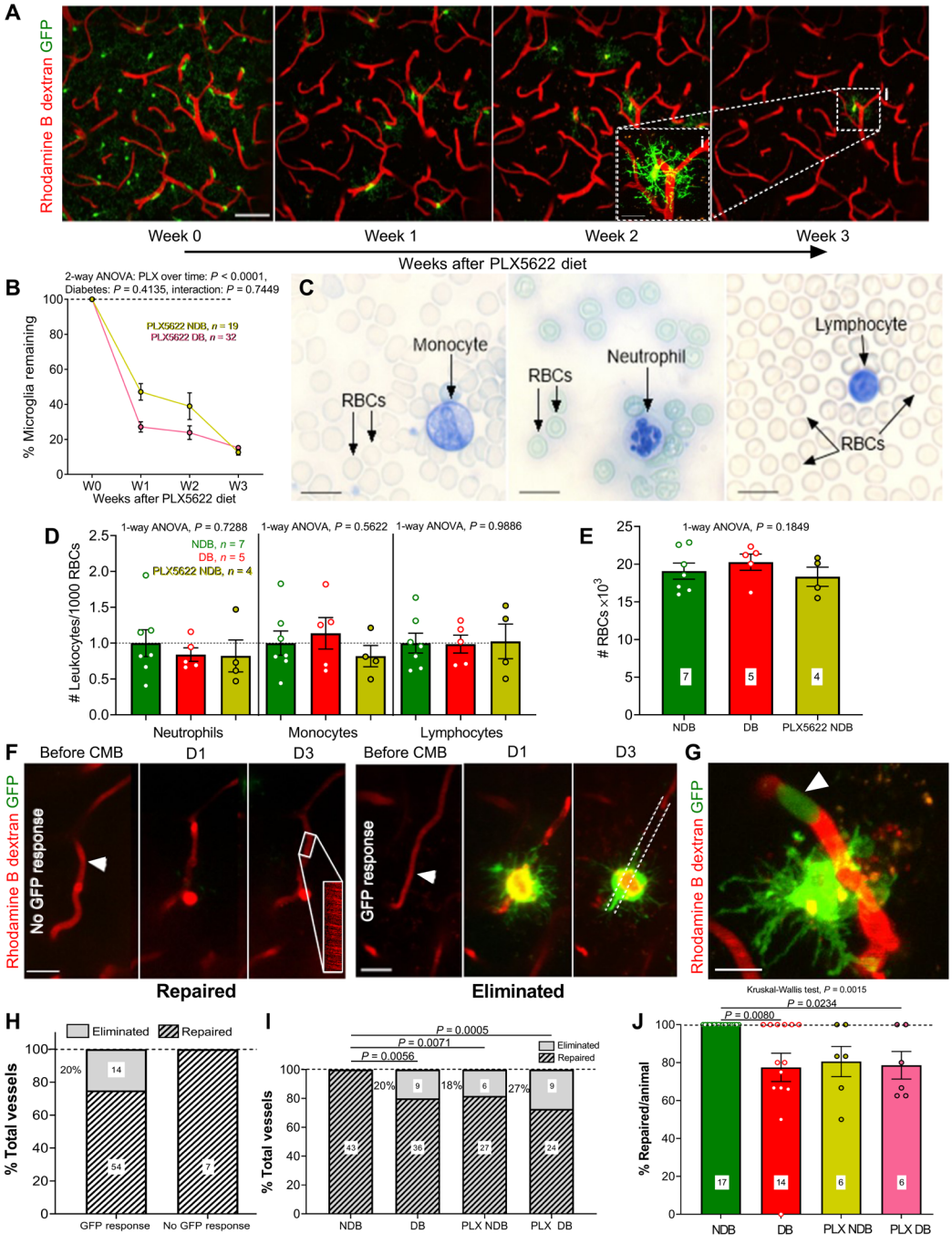

Fig. 3. Delayed appearance of GFP-expressing macrophages at the lesion site in microglia-depleted mice is associated with microvessel elimination. (**A**) In vivo images displaying PLX5622-mediated depletion of cortical microglia over 3 weeks. Inset shows remaining microglia. Scale bars, 50 and 20 μm, respectively. (**B**) Percentage microglia remaining following PLX5622 in NDB ($n = 19$ areas, six mice) and diabetic mice ($n = 32$ areas, six mice). (**C**) Bright-field images of a blood smear show monocytes (large-sized and abundant pale blue cytoplasm), neutrophils (dark blue, multilobed nuclei), and lymphocytes (dark nuclei and thin ring of cytoplasm). Scale bars, 20 μm. (**D**) Graphs show that PLX5622 treatment did not influence blood leukocytes numbers (normalized per 1000 RBCs). (**E**) Average number of RBCs per group (number of mice shown in each bar). (**F**) In vivo images of a microvessel before and after CMB (white arrowheads) in a PLX5622-treated mouse. CX3CR1 GFP cells would often appear at the bleed site (right; dashed lines show vessel loss). However, when no GFP cells appeared, microvessels were repaired and recanalized (inset line scan shows return of blood flow). Scale bars, 20 μm. (**G**) Image shows GFP-expressing leukocyte (white arrowhead) in the vascular lumen 1 day after CMB in PLX5622-treated NDB mouse. Scale bar, 20 μm. (**H**) Percentage of microvessels repaired or eliminated in PLX5622-treated mice as a function of whether GFP-expressing microglia/macrophages were present ("GFP response," $n = 85$) or absent ("no GFP response," $n = 7$) at CMB. (**I**) Percentage microvessels that were repaired or eliminated in PLX5622-treated NDB and diabetic mice ($n = 33$ vessels, six mice per group). (**J**) Percentage of vessels repaired per animal in NDB and diabetic PLX5622-treated groups. NDB and diabetic mice fed standard diet are shown for comparison. Statistics: Two-way mixed-effects model ANOVA (B), one-way ANOVAs (D and E), chi-squared analysis (I), and Kruskal-Wallis test with post hoc Dunn's multiple comparisons test (J). Error bars represent means ± SEM.

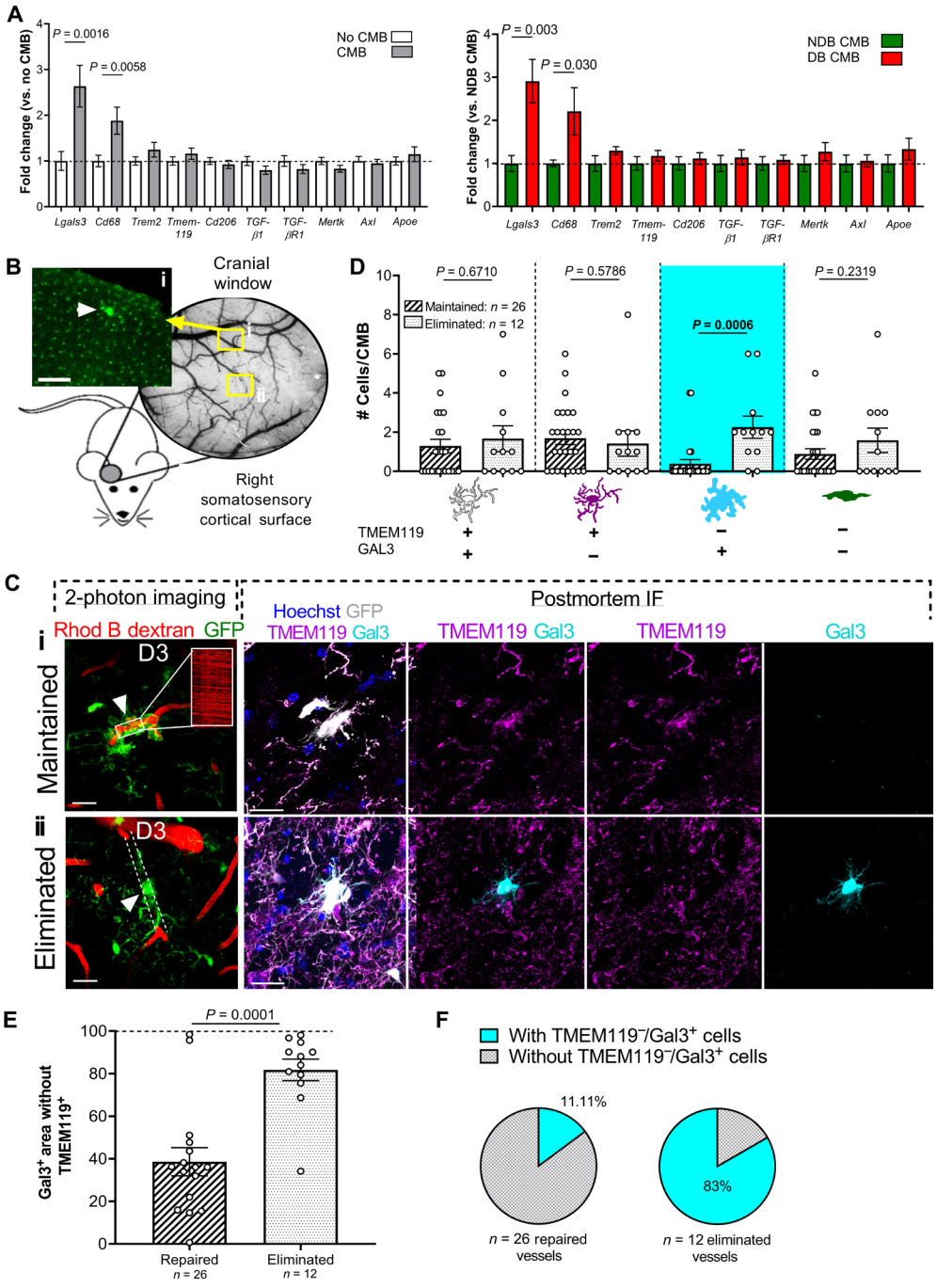

Fig. 4. Gal3 is up-regulated following CMBs in diabetic brain and expressed in macrophages associated with microvessel elimination. (**A**) Quantitative polymerase chain reaction (qPCR)–based detection of gene expression changes in the cerebral cortex showing the effect of CMBs (left) or DB (right). All tissue was collected 3 days after CMB, with nine mice per group. (**B**) Illustration showing the staggering of CMBs induced in the right somatosensory cortex of diabetic and NDB mice. Following in vivo confirmation of repair or elimination of microvessels at bleed sites, the same areas were identified in postmortem brain sections via their coordinates and presence of GFP aggregation (white arrowhead denotes CMB in coronal brain section from CX3CR1 GFP mouse). Scale bar, 100 μm. (**C**) Representative in vivo two-photon and postmortem confocal images at day 3 showing the expression of GFP, TMEM119, or Gal3 at sites of microvessel repair in a NDB mouse (i) or elimination in a diabetic mouse (ii). Note the presence of a TMEM119^{-}/Gal3^{+} cell at the bleed site when the microvessel was eliminated but not when it was maintained. White arrowheads denote site of CMB induction. Scale bars, 20 μm. IF, immunofluorescence. (**D**) Graph comparing the abundance and phenotype of cells at each CMB site expressing the following: TMEM119^{+}/Gal3^{+} (white), TMEM119^{+}/Gal3^{-} (purple), TMEM119^{-}/Gal3^{+} (cyan), and TMEM119^{-}/Gal3^{-} (green). Note the increased abundance TMEM119^{-}/Gal3^{+} (cyan) at CMB sites associated with vessel elimination. Data were pooled from five diabetic (23 imaging areas) and four NDB (15 imaging areas) mice, and two to five CMBs were induced per animal. (**E**) Bar graph showing average area of Gal3^{+} immunostaining that did not colocalize with TMEM119 in CMBs that were either repaired or eliminated. (**F**) Pie charts visualizing the proportion of repaired (left) or eliminated (right) microvessels that were associated with TMEM119^{-}/Gal3^{+} cells. Unpaired Student's *t* tests assessed differences between groups for graphs (A, D, and E). Error bars represent means ± SEM.

coordinates of the microbleeds induced in vivo to locate the same CMB sites in postmortem tissue (Fig. 4, B and C). Confocal imaging of cellular responses to CMBs revealed a diverse collection of cells in the microbleed milieu that were indistinguishable from one another using in vivo two-photon imaging of GFP-expressing cells (Fig. 4C). By examining colocalization of TMEM119 and/or Gal3 markers in GFP-expressing cells at the site of the CMB (Fig. 4C), we identified cells with four different expression signatures: TMEM119 expressing resident microglia that express Gal3 or not (see white and purple cells in Fig. 4D), as well as TMEM119 negative cells that express Gal3 or not (see cyan and green cells in Fig. 4D). When examining which unique cell signatures were associated with vessel elimination, we found that, when a greater number of cells expressed Gal3, but not the resident microglia marker TMEM119, vessel outcomes were significantly shifted toward elimination rather than repair (see cyan cell in Fig. 4, C and D; unpaired Student's *t* test, $P = 0.0006$). Quantifying Gal3 expression area as a function of TMEM119 expression area further confirmed that when Gal3 was not colocalized with TMEM119, microvessels were more likely to be eliminated (Fig. 4E; unpaired Student's *t* test, $P < 0.0001$). Furthermore, binarizing microvessel outcomes (repaired versus eliminated) with the presence or absence of $TMEM119^-/Gal3^+$ cells showed that these cells were present in most cases when a vessel was eliminated, but not when it was repaired (Fig. 4F). In summary, these results indicate that the presence of Gal3 expressing cells that do not coexpress the brain-resident microglia marker TMEM119, indicative of these cells' peripheral origin, is strongly associated with microvessel elimination after CMB.

To further link Gal3 expressing cells with phagocytic activity at bleed sites, we quantified lipofuscin deposits as a general marker of phagocytic activity in cells expressing Gal3 with or without TMEM119 (Fig. 5A). Our analysis revealed that $Gal3^+/TMEM119^-$ cells exhibited significantly greater lipofuscin content relative to $Gal3^-/TMEM119^+$ cells, and, although they tended to contain more lipofuscin than their $Gal3^+/TMEM119^+$ counterparts, these groups did not differ statistically (Fig. 5B; one-way ANOVA, $F_{2,24} = 3.627$, $P = 0.0352$; Tukey's multiple comparison's test, $Gal3^+/TMEM119^-$ versus $Gal3^-/TMEM119^+$: $P = 0.0345$; $Gal3^+/TMEM119^-$ versus $Gal3^+/TMEM119^+$: $P = 0.1412$). Next, we injected adeno-associated virus (AAV1)-BR1-iCre into Ai9 reporter mice to induce cre-dependent td-tomato expression in vascular endothelial cells (*38*). One day after induction of injury, we observed degenerating vascular endothelial cells at damage sites surrounded by cells expressing the pan-microglia/macrophage marker ionized calcium binding adaptor molecule 1 (Iba1) or Gal3 (Fig. 5C). In some instances, suspected macrophage processes were observed enwrapping and segmenting the degenerating vascular endothelium (inset in Fig. 5C). Furthermore, we could detect engulfed deposits of endothelial td-tomato reporter protein within these macrophages (see white arrows in Fig. 5C). These findings support the idea that Gal3 expressing cells are particularly phagocytic and are capable of engulfing injured vascular endothelium (*17*, *18*).

Depletion of infiltrative Gal3 expressing macrophages prevents elimination of microvessels in diabetic mice

The fact that Gal3 is highly expressed in peripheral macrophages (*39*) and that Gal3 expressing cells at the lesion site did not coexpress the resident microglial marker TMEM119 suggested that they infiltrated the brain via the circulation. Therefore, to prevent the loss of capillaries after CMB, we depleted circulating macrophages in mice by intravenous injection of clodronate (CLR). When liposomes containing clodronate are engulfed by circulating phagocytic cells, the liposomes are degraded in the phagolysosome, releasing encapsulated clodronate and initiating apoptosis. As expected, CLR treatment significantly depleted monocytes and neutrophils in the blood (Fig. 6A) but did not affect lymphocytes or RBCs (unpaired Student's *t* test, $P = 0.10$). We also found that Gal3 expressing macrophages in the spleen were significantly reduced with CLR treatment (Fig. 6B and fig. S6A; unpaired Student's *t* test, $P = 0.0005$), whereas PLX5622 had no effect on these cells (Fig. 6B). Intravenous CLR treatment specifically targeted peripheral immune cells since we did not observe any changes in cerebral cortical microglial density with CLR, similar to other reports using rodent models (fig. S6, B and C; one-way ANOVA, $F_{2,29} = 0.6762$, $P = 0.5164$) (*40*).

Having confirmed that CLR effectively depleted cells in the circulation or peripheral organs that could give rise to infiltrative macrophages, we induced CMBs in diabetic mice treated with vehicle or CLR before the insult, on the day of CMB induction, and 2 days after CMB. First, we confirmed that CLR treatment significantly attenuated the infiltration of $Gal3^+/TMEM119^-$ macrophages at the lesion site in diabetic mice (Fig. 6, C and D; one-way ANOVA, $F_{2,87} = 14.48$, $P < 0.0001$; Tukey's multiple comparison's test, DB versus CLR DB: $P = 0.0344$). Notably, CLR did not affect the appearance of $TMEM119^+$ resident microglia (coexpressing Gal3 or not) at the lesion site (Fig. 6, C and D; one-way ANOVA, $F_{2,87} = 0.7862$, $P = 0.7862$). This finding provides further evidence that $TMEM119^+/Gal3^+$ cells that normally reside within the brain are not detrimental to repair, unlike the infiltrative $TMEM119^-/Gal3^+$ cells. CMBs in diabetic mice were associated with a significant increase in Gal3 immunostaining area that did not colocalize with the resident microglia marker TMEM119, which was reversed with CLR treatment (Fig. 6E; one-way ANOVA, $F_{2,62} = 45.49$, $P < 0.0001$; Tukey's multiple comparison's test, DB versus CLR DB: $P < 0.0001$).

To further understand the effects of CLR on phagocytic activity and related signaling proteins at bleed sites, we imaged and quantified lipofuscin content as well as CD68, and triggering receptor expressed on myeloid cells 2 (TREM2) (*41*) immunofluorescence at CMBs, markers that were elevated in our gene expression analysis (see Fig. 4A). Our analysis revealed that CLR treatment in diabetic mice significantly reduced the area of lipofuscin signal associated with GFP-expressing cell aggregates at the site of the CMB relative to vehicle-treated diabetic mice (Fig. 6F; one-way ANOVA, $F_{2,121} = 4.313$, $P = 0.0366$; Tukey's multiple comparison's test, DB versus CLR DB: $P = 0.0236$). Since immunofluorescence staining protocols for Gal3 were incompatible with CD68 and TREM2 (due to requirements for heating associated with antigen retrieval or primary antibody host mismatches), we present data for each protein separately. CLR treatment in diabetic mice significantly reduced the percent area of CD68 immunostaining at the lesion site (Fig. 6, G and H; one-way ANOVA, $F_{2,51} = 5.857$, $P = 0.0051$; Tukey's multiple comparison's test, NDB versus DB: $P = 0.0222$; DB versus CLR DB: $P = 0.0078$), but not the number of CD68 puncta (Fig. 6I; number of CD68 puncta: one-way ANOVA, $F_{2,51} = 0.4932$, $P = 0.6135$). TREM2 expression was also elevated in diabetic CMBs, and this expression was significantly reduced with CLR treatment (Fig. 6, J and K; one-way ANOVA, $F_{2,51} = 7.112$, $P = 0.0019$; Tukey's multiple comparison's test, NDB versus DB: $P = 0.0058$; DB versus CLR DB: $P = 0.0051$). These findings show that DB is associated with increased phagocytic activity and TREM2 protein expression at bleed sites, both of which can be reduced and effectively normalized to healthy control levels with CLR treatment.

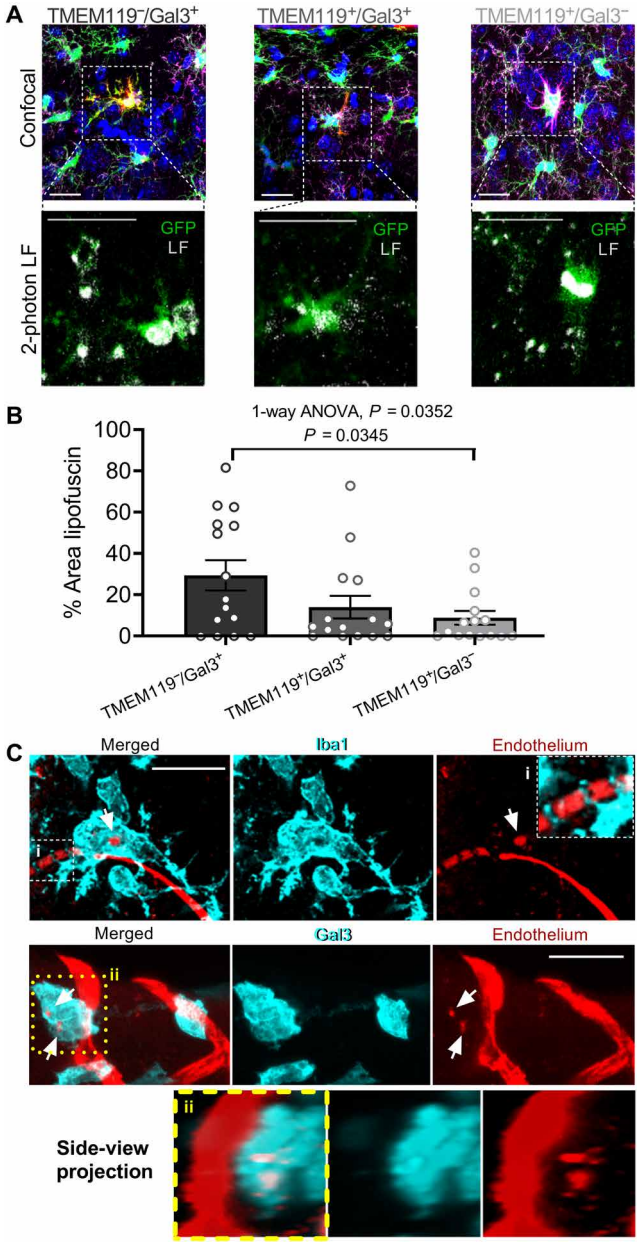

Fig. 5. Phagocytic activity is elevated in Gal3 expressing cells. (**A**) Top: Confocal immunofluorescent imaging of brain sections from diabetic mice reveals cells expressing various combinations of CX3CR1 GFP (green), TMEM119 (purple), Gal3 (red), or Hoechst (blue). Here, we identified three populations of cells expressing the following: TMEM119$^-$/Gal3$^+$, TMEM119$^+$/Gal3$^+$, or TMEM119$^+$/Gal3$^-$. Bottom: The same sections were then imaged at 750 nm of wavelength on the two-photon microscope to detect lipofuscin (LF, lipofuscin) signal (see white puncta in the bottom row of images). Scale bars, 20 μm (top) and 10 μm (bottom). (**B**) Quantification of lipofuscin signal within GFP cells binned according to their expression of TMEM119 and/or Gal3. (**C**) Maximum intensity projection showing an Iba1 (left)– or Gal3 (right)–expressing macrophage engulfing td-tomato–labeled endothelium (white arrows) following CMB. (i) Highlights macrophage processes segmenting the degenerating endothelium. (ii) Side view (*y-z*) projection showing the engulfment of td-tomato–labeled endothelium by a Gal3 expressing macrophage. Scale bars, 20 μm. One-way ANOVA and post hoc Tukey's multiple comparisons test were used to compare the amount of lipofuscin observed in different cells (A). Error bars represent means ± SEM.

To test our hypothesis that Gal3 expressing macrophages were a primary factor in dictating vessel outcomes in vivo, we imaged CX3CR1 GFP–expressing microglia/macrophage responses and microvessel fates over 2 weeks following induction of CMBs in NDB and diabetic mice treated with or without CLR (Fig. 7A). These experiments revealed that CLR treatment in diabetic mice significantly reduced the fraction of microvessels that were eliminated after CMB relative to untreated diabetic mice (5% versus 29%; Fig. 7, A and B). These same trends were observed when averaging the percentage of vessels repaired versus eliminated across mice (Fig. 7C). It is worth noting that the two instances of vessel elimination in the diabetic CLR-treated group (2 of 37 vessels) came from only one mouse, and the remaining seven diabetic mice treated with CLR all showed 100% repair of microvessels after CMB (Fig. 7, B and C). Together, these in vivo experiments indicate that CLR prevents Gal3 expressing macrophages from infiltrating bleed sites and eliminating microvessels in diabetic mice.

DISCUSSION

In the present study, we used two-photon and confocal microscopy to characterize the long-term repair of CMBs and the evolving immune cell responses to these insults over a 14-day period in a mouse model of type 1 DB (see summary in Fig. 7D). Following CMB, ~20 to 29% of ruptured capillaries were lost in the diabetic group, a phenomenon that was not observed in healthy animals that exhibited repair of all damaged microvessels and their lasting reintegration into the cerebral circulation. Although physical characteristics of the aggregated CX3CR1 GFP–expressing cells at the bleed site did not differ between groups (i.e., in terms of area of GFP expression and coverage along the vessel), markers of phagocytic activity and the diverse composition of cells associated with repaired and eliminated microvessels were distinctive. Specifically, eliminated microvessels in the diabetic cortex attracted Gal3$^+$ macrophages that did not express the resident/homeostatic microglia marker TMEM119. This unique population of cells was mostly excluded from the CMB response in diabetic mice treated with intravenous CLR, coincident with improved microvascular repair rates and reduced phagocytic activity. Together, these findings identify a cellular target associated with the pathological elimination of microvasculature in DB that can be modulated via depletion of invasive macrophages.

The heterogeneity of microglia and brain macrophages under homeostatic and disease conditions has been increasingly highlighted by recent publications (*42*–*44*). Here, we sought to further define the microglia/macrophage population at microvascular bleed sites by examining colocalization of CX3CR1 GFP, CD206, TMEM119 (*28*), and Gal3. Our initial attempts to understand which cells invaded the bleed site revealed that CD206-expressing meningeal and perivascular macrophages, which usually reside on the pial surface or along penetrating vessels, were not participating in the response. This is perhaps expected given the depth of bleeds induced (50 to 100 μm from the surface) and the considerable migratory distance that would be required. On the basis of recent reports showing that Gal3 expressing microglia/macrophages are resistant to chronic PLX5622 treatment (*35*), in tandem with our time-lapse imaging experiments showing that a PLX5622-resistant cell population could appear at bleed sites 24 hours after induction, we turned our attention toward Gal3 expressing cells. Although Gal3 was originally identified on peripheral inflammatory macrophages, several studies

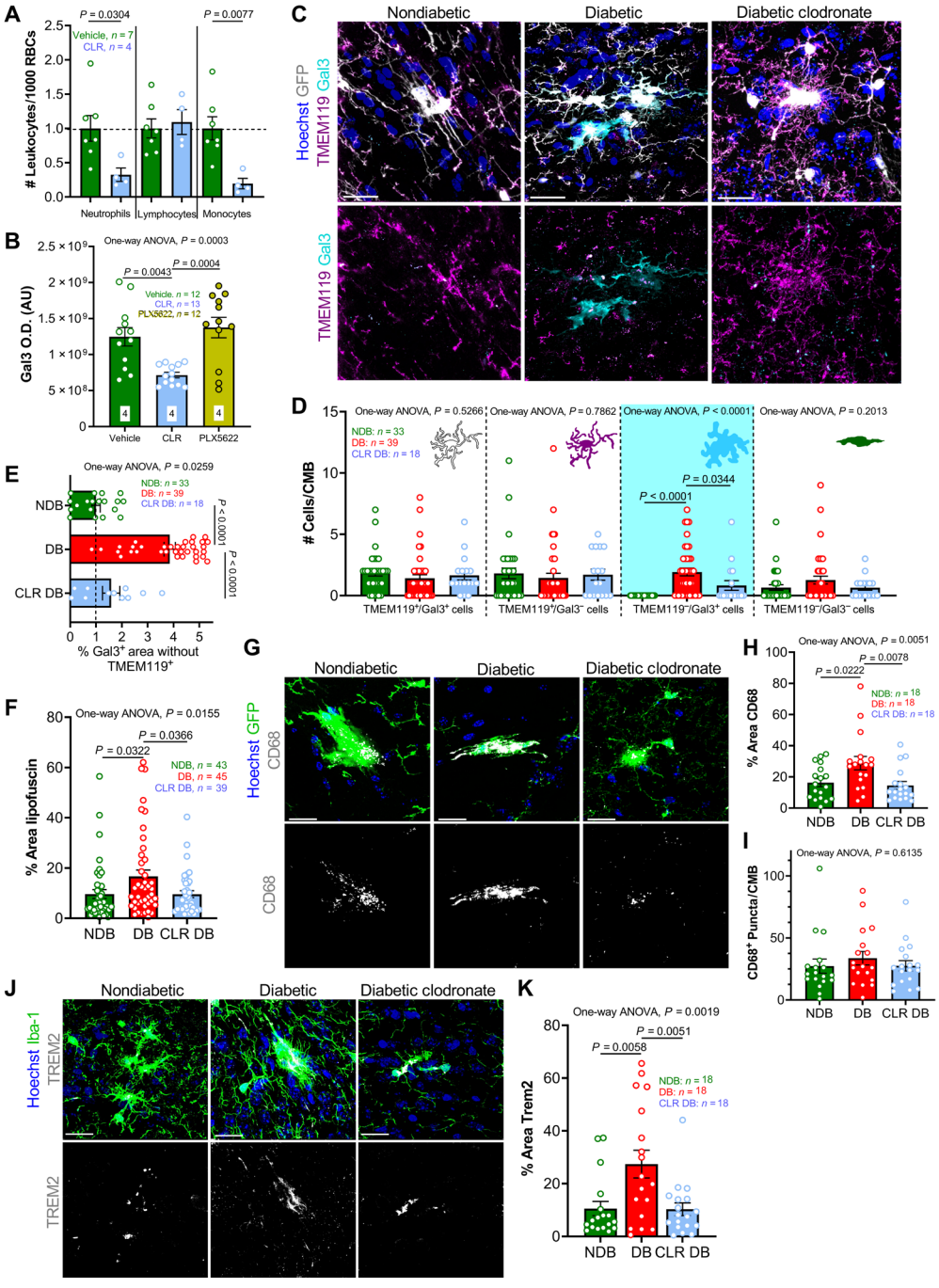

Fig. 6. Clodronate treatment depletes peripheral immune cells, attenuates the infiltration of TMEM119$^-$/Gal3$^+$ cells, and reduces phagocytic activity at bleed sites. (**A**) Quantification of neutrophils, lymphocytes, and monocytes, normalized to RBCs, from blood smears in vehicle- and CLR-treated ($n = 4$ mice per group) mice. (**B**) Graph showing the effect of clodronate or PLX5622 on optical density (O.D.) of Gal3 expressing macrophages in spleen ($n = 4$ mice per group). AU, arbitrary units. (**C**) Confocal images showing expression of Gal3, TMEM119, and Hoechst 33342 expression 3 days after CMB. Scale bars, 20 μm. (**D**) Quantification of cell numbers and phenotype based on expression of TMEM119 and/or Gal3 at bleed sites in NDB ($n = 8$), diabetic ($n = 10$), and clodronate-treated diabetic mice ($n = 6$). (**E**) Percent area of Gal3$^+$ immunostaining that does not colocalize with TMEM119 in NDB ($n = 33$ CMB from 8 mice), diabetic ($n = 39$ CMB from 10 mice), and clodronate-treated diabetic ($n = 18$ CMB from 6 mice) groups. Data were normalized to NDB values. (**F**) Quantification of lipofuscin at CMBs in NDB ($n = 43$ CMB from 17 mice), diabetic ($n = 45$ CMB from 14 mice), and clodronate-treated diabetic mice ($n = 39$ CMB from 8 mice). (**G**) Confocal images show expression of CD68 within GFP-expressing cells 3 days after CMB. Scale bars, 20 μm. (**H**) Graph showing percent area of CD68 colocalization with GFP-expressing cells at CMBs from NDB ($n = 16$ CMBs from six mice), diabetic ($n = 18$ CMBs from six mice), and clodronate-treated diabetic ($n = 18$ CMBs from six mice) mice. (**I**) Number of CD68 particles within GFP cells at each CMB. (**J**) Confocal images showing immunofluorescent staining for Iba1 and TREM2 3 days after CMB. Scale bars, 20 μm. (**K**) Percent area of TREM2 immunostaining at CMBs in NDB, diabetic, and clodronate-treated diabetics ($n = 6$ mice per group). Statistics based on unpaired Student's t test (A) or one-way ANOVAs with post hoc Tukey's multiple comparisons tests (B, D to F, H, I, and K). Error bars represent means ± SEM.

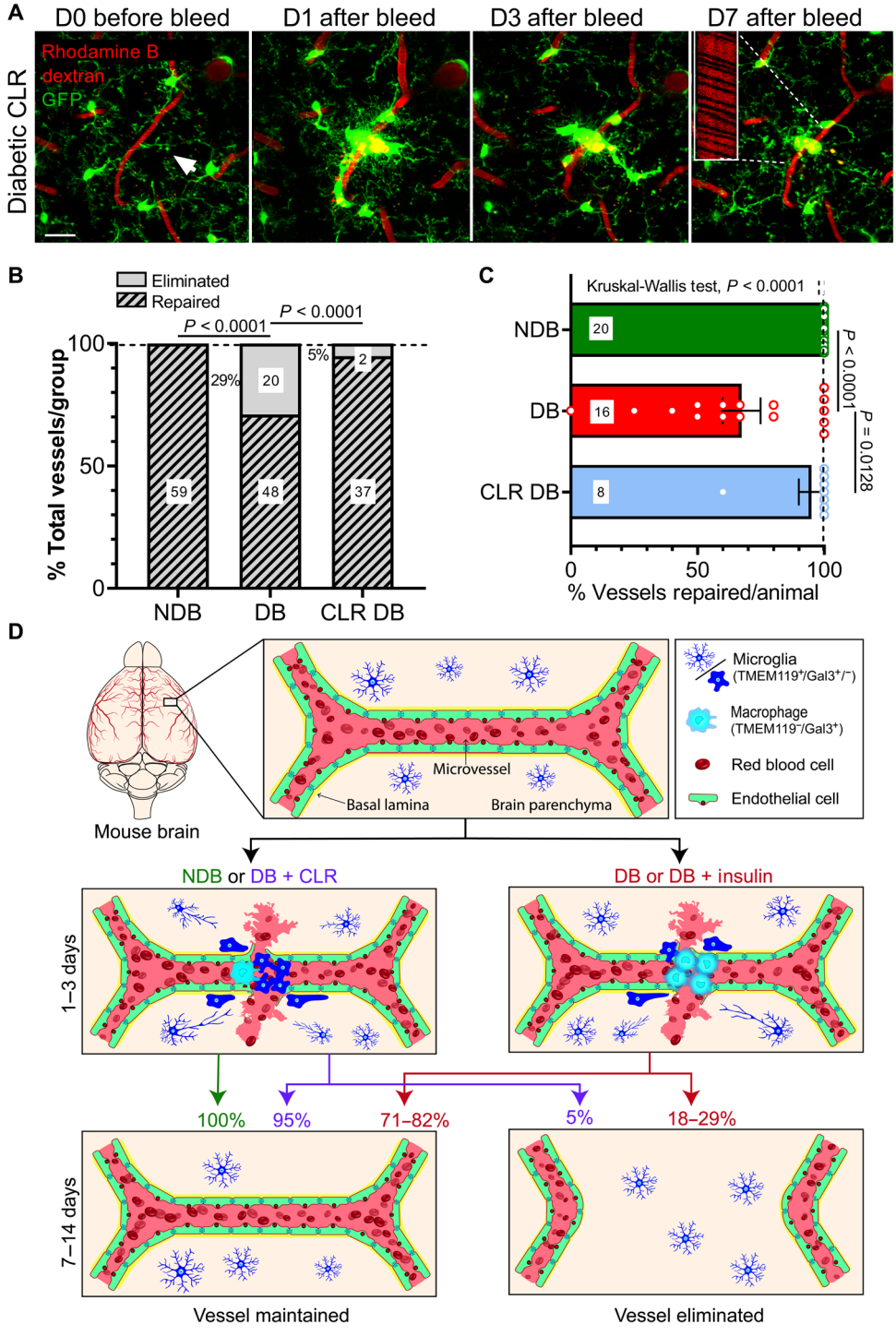

Fig. 7. Depletion of circulating macrophages with clodronate prevents vessel loss after CMB in diabetic mice in vivo. (**A**) Representative time-lapse in vivo images illustrating the CX3CR1 GFP–expressing microglia/macrophage response to CMB and subsequent repair and maintenance of a damaged microvessel labeled with rhodamine B dextran in a diabetic mouse treated with CLR. Scale bar, 20 μm. (**B**) Graph summarizing the percentage of microvessels that were repaired or eliminated following induction of CMB in NDB ($n = 20$), diabetic ($n = 16$), or clodronate-treated diabetic ($n = 8$) mice. (**C**) Percentage of microvessels repaired per animal within each experimental group. Note that each mouse received one to five CMBs. (**D**) Illustration summarizing the principle findings of our study. Data were analyzed using chi-squared analysis (B) or nonparametric Kruskal-Wallis test with post hoc Dunn's multiple comparisons test (C). Error bars represent means ± SEM.

have documented the presence of Gal3 expressing cells in the injured brain and mouse models of vascular dementia (*45*, *46*). For example, the Kriz laboratory and others have shown that Gal3 is expressed by proliferative resident microglia that minimize brain damage after ischemic stroke in NDB/healthy mice (*47*, *48*). We also found Gal3 expressing cells at bleed sites, as well as in the uninjured hemisphere of both NDB and diabetic mice. However, a key consideration was whether the Gal3$^+$ cell also expressed the resident/homeostatic microglia marker TMEM1119. Under diabetic conditions, when vessels were eliminated, most recruited cells were Gal3$^+$/TMEM119$^-$, whereas repaired vessels rarely contained these cells. Gal3 expression has paradoxically been associated with both protective (*47*–*49*) and degenerative (*25*, *26*, *50*–*52*) roles in various injury and disease contexts. For example, Pugliese *et al.* (*49*) showed that Gal3 knockout in diabetic mice exacerbated functional renal degeneration and pathological structural changes in glomeruli, including increased expression of extracellular matrix components and mesangial thickening, resulting from impaired scavenging of advanced glycation end products. Conversely, others have noted that Gal3 expression is associated with phagocytic microglia/macrophages and contributes to the pathological removal of synapses and axonal tracts during aging (*26*), traumatic brain injury (*51*), and neurodegenerative diseases (*25*, *50*). These seemingly duplicitous functions may be attributed to the fact that Gal3 is present in disparate subcellular compartments (including the cytoplasm, nucleus, extracellular space, etc.) and can be modulated through various posttranscriptional modifications (*53*), thus enabling diverse signaling mechanisms and functions depending on the specific disease, injury, or tissue studied. To better resolve this question and identify which Gal3 expressing leukocytes mediate vessel loss, future studies using cell-specific cre-driver lines crossed with Gal3 floxed mice are certainly warranted.

In the context of microvascular elimination, Gal3 signaling may act through several pathways in infiltrative leukocytes to drive this outcome. Notably, activated peripheral leukocytes, including monocytes and neutrophils, are known to secrete Gal3 that serves as an endogenous ligand for Toll-like receptor 4 (TLR4) (*52*). Activation of TLR4 amplifies local inflammation through initiation of proinflammatory nuclear factor κB and caspase (3/7 and 8) signaling, increased cytokine production, and inducible nitric oxide synthase (iNOS) generation (*52*). Functioning in both autocrine and paracrine modalities, Gal3 promotes the development of classically activated macrophages and up-regulates expression of interleukin-12, tumor necrosis factor–α, and iNOS in target cells (*54*). Infiltrative leukocytes that highly express iNOS may be particularly relevant to microvessel loss in diabetic mice, given that they are associated with demyelinating lesions and tissue damage in a mouse model of multiple sclerosis (*55*). Microvascular dysfunction (specifically, the loss of functional hyperemia) in the diabetic retina has also been specifically linked to increased iNOS expression that can be mitigated with iNOS inhibitors (*56*). Future work investigating the protective effects of blocking the downstream targets of Gal3 signaling, such as an iNOS inhibitor, would provide additional insight into the molecular mechanisms by which Gal3 expressing macrophages contribute to microvascular elimination.

The highly phagocytic nature of infiltrative Gal3 expressing macrophages may explain why they are associated with vessel elimination. In particular, Gal3 was recently identified as an endogenous TREM2 ligand and has been shown to modulate phagocytosis of β-amyloid protein in a mouse model of Alzheimer's disease (*57*). The implication that recruited Gal3$^+$/TMEM119$^-$ macrophages at injury sites are highly phagocytic is supported by our data, highlighting the presence of engulfed endothelial debris in these cells, as well as increased intracellular lipofuscin content. Furthermore, we noted that the elevated expression of TREM2 (a protein required for microglia/macrophage phagocytosis) (*10*) at diabetic bleed sites could be reduced to normal levels by depleting Gal3 expressing macrophages with clodronate. These macrophages could conceivably represent the same population of Iba1$^+$/CX3CR1 GFP–expressing macrophages that line the penumbra and engulf microvessels after stroke (*21*). We also note that our results do not necessarily conflict with previous studies, showing that macrophages play a role in repairing damaged blood vessels (*15*), since other macrophages (e.g., GFP$^+$ cells that did not express Gal3) were present at the bleed site. For example, we observed Gal3$^-$/TMEM119$^-$/GFP$^+$ cells at CMB sites that could aid in repair; however, we did not find them significantly associated with a particular vessel outcome (see Fig. 4). In summary, while Gal3$^+$/ TMEM119$^+$ cells that normally reside within the brain parenchyma may serve a protective role in response to injury, our data indicate that Gal3$^+$/TMEM119$^-$ macrophages recruited to injury sites, especially in a chronic disease state such as DB, are highly phagocytic and promote the elimination of microvessels.

An interesting question raised by our study concerns the source of the Gal3$^+$/TMEM119$^-$ cells recruited to injury sites in the diabetic brain. While providing a definitive answer to this question is very difficult given the highly mutable gene expression profiles and morphology of microglia/macrophages and their mobility from blood to brain and vice versa (*58*), our data argue that they arise from the circulation. First, when imaging CMBs following microglia depletion, we found that CX3CR1 GFP–expressing cells would appear at the lesion site within 24 hours, fitting with the time frame for circulating monocyte/macrophage invasion described in previous microbleed and ischemic stroke studies (*12*, *58*, *59*). Furthermore, there are previous reports suggesting that the diabetic brain is especially permissive to immune cell infiltration given that endothelial cells exhibit increased expression of adhesion proteins involved in the leukocyte transmigration pathway (*60*) and greater BBB permeability after stroke or microbleed (*3*, *8*, *61*). It is also for this reason that we opted against doing bone marrow transplant experiments, which are not easily tolerated even in healthy mice and are known to disrupt the BBB and lead to the artificial recruitment of macrophages; these issues would therefore further complicate any conclusions about the source of recruited cells. Second, Gal3$^+$ cells recruited to injury sites did not express TMEM119, which previous studies have shown is highly specific to microglia and not peripheral or brain-residing macrophages (*28*). Although there is evidence that TMEM119 expression can change in disease states (*37*), we did not detect a significant change in gene expression with induction of CMB or DB (see Fig. 4A), and we were always able to detect TMEM119 immunostaining in cells surrounding microbleeds. Lastly, we showed that intravenous clodronate administration, could deplete circulating monocytes/macrophages and prevent the recruitment of Gal3$^+$/TMEM119$^-$ cells to the bleed site without affecting resident microglia expressing TMEM119. Despite the evidence supporting a peripheral source for Gal3$^+$/TMEM119$^-$ cells, we acknowledge the possibility that a clodronate-sensitive Gal3$^+$/TMEM119$^-$/CD206$^-$ macrophage, perhaps from the meningeal surface, could migrate to the bleed site, similar to what has been described for skull-derived neutrophils after stroke (*62*). Future fate mapping time-lapse imaging

studies using Gal3 and TMEM119 reporter mice would be needed to resolve this question definitively.

The present data suggest that diabetes enhances the infiltration of phagocytic macrophages at injury sites. While our study is the first to describe such a phenomenon in the diabetic brain, at least to our knowledge, it is reminiscent of other studies showing that certain disease states or injuries are accompanied by the invasion of monocyte-derived macrophages and neutrophils that contribute to neuropathology (*63*, *64*). For example, in animal models of multiple sclerosis, infiltrative monocytes promote neuroinflammation, are highly toxic to neurons, and are strongly associated with disease progression (*65*–*67*). However, an unresolved question from our current work pertains to why the diabetic condition would enhance the recruitment of macrophages. Previously, we showed that a chronic perturbation in interferon-γ signaling in type 1 DB diminishes acute microglial envelopment of microbleeds (within 1 hour) and exacerbates BBB disruption (*8*). It is conceivable that greater, persistent BBB permeability after injury may enhance the release of chemotactic signals and thus promote the recruitment of circulating immune cells. Another possibility is that the chronic low-grade inflammation associated with type 1 DB may alter how resident microglia interact with, and potentially restrict, the entry of infiltrative macrophages (*68*, *69*). For instance, microglia activated by demyelinating lesions are enriched with interferon signaling genes that may serve to limit the invasion of circulating monocytes (*32*). In this context, studies using single-cell transcriptomics of resident microglia and putative macrophages (i.e., $Gal3^{+}$/$TMEM119^{-}$) at diabetic bleed sites could further define molecular mechanisms that promote vessel elimination.

The notion of vessel repair is unquestionably a complex process involving multiple cell types associated with the neurovascular unit. In the present work, we opted for a decidedly simplistic concept of repair and binarized the outcome of microvessels damaged by CMBs. Specifically, a vessel was designated as repaired when it regained blood flow and persisted for the entire 14-day imaging period; conversely, vessels were "eliminated" when they failed to regain blood flow (based on the absence of streaking RBCs in the blood plasma) and essentially disappeared, given that there were no traces of intraluminal fluorescent dextran in the capillary segment. We reasoned that the preservation and recanalization of microvessels, invariably noted in healthy, NDB CX3CR1 mice (note that repair rates could vary across mouse strains), was a reparative response. While one could argue that the loss of microvessels in diabetic mice could also be reparative in acute injury, the long-term impact of microvascular elimination could compound over time and have deleterious consequences. Type 1 DB is a known risk factor for micro- and macrovascular dysfunction, and human imaging studies have highlighted extensive functional and anatomical cerebrovascular pathology in this disease, including increased incidences of CMBs (*6*, *7*). Indicative of permanent cerebral vascular damage, as few as four coincident CMBs have been correlated with cognitive impairment (*5*). The heightened propensity for microvascular injury and loss under the diabetic condition that we describe may help support clinical reports of impaired cerebral blood flow regulation and progressive, aging-related deterioration of cognitive function (*70*). Notably, Van Duinkerken *et al.* (*71*) identified a significant correlation between the prevalence of microangiopathy in patients with type 1 DB and reduced functional connectivity assessed using functional magnetic resonance imaging techniques. In this context, the prevention of microvascular loss after injury in diabetic mice with CLR administration merits further research to assess its therapeutic potential in mitigating cerebrovascular pathology.

MATERIALS AND METHODS

Animals

Animals involved in this study were used and cared for in accordance with approved guidelines set forth by the University of Victoria Animal Care Committee and the Canadian Council on Animal Care. Reporting of this work complies with ARRIVE guidelines. Two- to 3-month-old male $CX3CR1^{+/GFP}$ mice [research resource identifiers (RRID): IMSR_JAX:005582] on a C57BL/6J background (RRID: IMSR_JAX:000664) were used in all experiments (*72*). As previously reported by our group, there are no significant differences between microglial responses to CMBs in mice heterozygous for the *Cx3cr1* gene relative to those with both *Cx3cr1* alleles intact (*8*). Animals were group-housed on ventilated racks in a humidity-controlled (40 to 50% relative humidity) and temperature-controlled (21° to 23°C) facility with a 12-hour light/12-hour dark cycle and given ad libitum access to food and water. For microglia depletion experiments, PLX5622 diet (1200 ppm), generously provided by Plexxikon, was substituted for regular irradiated mouse chow (AIN-76A, Research Diets). Mice were given ad libitum access to the PLX5622 diet 3 weeks before in vivo imaging and received the diet throughout the remainder of the experiment.

Surgical procedures

For the experiments described in this study, two surgical procedures were used: a chronic cranial window implantation for longitudinal in vivo two-photon microscopy and a thin skull preparation for generating tissue with CMBs for immunofluorescent staining and confocal microscopy. In all preparations, mice were anesthetized using gaseous isoflurane (2% for induction and 1.3% for maintenance) in medical air (80% N_2 and 20% O_2) at a flow rate of 0.7 liter/min and head-fixed in a custom surgical stage. A temperature feedback regulator and rectal probe thermometer maintained the animals' body temperature at 37°C throughout the procedure. A 0.03-ml bolus of lidocaine was injected subcutaneously at the surgery site and allowed to diffuse for several minutes before an incision was made. Mice implanted with a chronic cranial window also received a 0.03-ml intramuscular injection of 2% dexamethasone to reduce acute inflammation resulting from the procedure.

Chronic cranial windows were installed on mice 5 weeks before beginning in vivo two-photon imaging. An incision was made along the midline of the scalp, and a custom metal ring (outer diameter, 11.3 mm; inner diameter, 7.0 mm; height, 1.5mm) was positioned over the right somatosensory cortex and secured to the skull with Krazy Glue. A circular area (diameter, ~4 mm) within the metal ring was thinned using a high-speed dental drill, and cold Hepes-buffered artificial cerebrospinal fluid (ACSF) was applied regularly to the skull during the drilling procedure to cool the area. Fine forceps were used to remove the thinned skull fragment, and gel foam soaked in cold ACSF was used to moisten the exposed brain; the dura was kept intact. A 5-mm no. 1 thickness coverslip was placed over the craniectomy and secured to the skull using Krazy Glue and dental cement. Mice were allowed to recover under a heat lamp and monitored regularly before being returned to their home cages.

Thin skull surgical procedures were performed on the day of CMB induction. A square area of ~16 mm^2 was thinned over the right somatosensory cortex using a high-speed dental drill, and cold ACSF was applied to the skull intermittently during the procedure. When small meningeal blood vessels became visible through the skull upon addition of ACSF, the drilling procedure was deemed complete. Isoflurane anesthesia was reduced to 1% in medical air, and the mouse was immediately transferred to a custom-built imaging stage on the two-photon microscope for CMB induction, as described below. After 8 to 10 CMBs were induced per animal, separated by at least 250 μm, the scalp was sutured closed and the mouse was then returned to its home cage for 3 days before it was euthanized and processed for immunofluorescence.

DM induction and treatment groups

Mice were randomly assigned to treatment groups: NDB, diabetic, and insulin-treated diabetic. Following cranial window implantation, and 4 weeks before in vivo two-photon imaging, mice were fasted for 5 hours before they received intraperitoneal injections staggered over 3 to 4 days of either vehicle or STZ (75 mg/kg) in sodium citrate buffer (pH 4.5) to induce DB. This protocol of administering multiple low doses of STZ minimizes the possibility of any direct toxic effects of STZ on the brain. Mice were given ad libitum access to 5% sucrose water for the first day following STZ injection to prevent acute hypoglycemia. Type 1 DM onset was confirmed 1 week following the first STZ injection by using an Aviva Accu-Chek blood glucose meter on a drop of blood from the tail vein of treated mice. Similar to previous work (*8*), mice with blood glucose values of ≥15.0 mM were defined as diabetic. Mice that had received STZ injections but did not exceed the hyperglycemic threshold were given a single, additional dose of STZ. NDB mice consisted of animals that failed to surpass the hyperglycemic threshold following the top-up dose of STZ and mice that were fasted and received equivalent injections of vehicle. The subset of confirmed diabetic mice assigned to receive insulin treatment was implanted with slow-release insulin pellets (0.1 U/24 hours; LinBit, LinShin Canada Inc.) 1 week after confirmation of DM. To implant the pellets, mice were lightly anesthetized with isoflurane (1 to 1.3%) in medical air and received a 0.03-ml bolus of subcutaneous lidocaine injected between the shoulder blades. A small incision was made in the skin at the injection site, and the insulin pellet(s) were inserted between the skin and the muscle tissue. The incision was sutured shut, and the mouse was regularly monitored as it recovered under a heat lamp.

For drug intervention experiments, mice received intravenous CLR (50 mg/kg; Liposoma B.V.) 2 days before CMB induction, on the day of CMB induction, and 2 days later. This treatment regimen ensured sustained depletion of peripheral macrophages. Diff-Quik histological staining confirmed depletion of circulating immune cells in treated animals.

In vivo two-photon imaging and CMB induction

Mice were lightly anesthetized with isoflurane (~1% in medical air) and received intravenous administrations of 0.1 ml of rhodamine B dextran (Sigma-Aldrich; 4% in sterile saline or CLR solution for intervention experiments) to permit visualization of the vasculature. High-resolution two-photon images of GFP-expressing microglia/macrophages and vasculature in the somatosensory cortex were acquired in vivo using an Olympus FV1000MPE laser scanning microscope fed by a mode-locked Ti:Sapphire laser source (Mai Tai XF DeepSee, Spectra-Physics) and equipped with a water-dipping 40× objective lens [Olympus; numerical aperture (NA) = 0.8]. Fluorescence or autofluorescence imaging was achieved by tuning the laser to 750 nm (lipofuscin), 880 nm (for rhodamine B dextran and GFP excitation), or 900 nm (Cy5). Emitted light was split by a dichroic filter (552 nm) before it was directed through band-pass filters (495 to 540 nm and 558 to 706 nm). *Z*-stacks of 45 μm in depth were composed of individual images of 144 μm by 144 μm (1024 by 1024 pixel resolution) collected at 1.5-μm *z*-step intervals. Each image acquired was the product of three averaged images per plane (Kalman = 3 frames). Vessel landmarks and imaging coordinates were used to image the same areas on the day of CMB induction (D0) and 1, 3, 7, and 14 days thereafter.

As previously described (*8*), microbleeds were induced by targeting the center of a flowing microvessel (3 to 6 μm in width), 50 to 100 μm below the cortical surface, with the two-photon laser (850 nm, ~220 mW at the back aperture) for a period of ~6 s. CMBs were induced at least 250 μm apart. Successful vessel rupture was confirmed by extravasation of fluorescent plasma immediately following cessation of the induction protocol. A single, in-plane image was acquired to record the rupture of the microvessel.

Immunofluorescent staining and imaging

Mice were euthanized with sodium pentobarbital (Euthanyl diluted 1:1 in sterile saline; Bimeda-MTC Animal Health Inc.) and transcardially perfused with 10 ml of 0.1 M phosphate-buffered saline (PBS), followed by 10 ml of 4% paraformaldehyde (PFA) in 0.1 M PBS. Whole brains and spleens were extracted and fixed overnight in 4% PFA. Brains were then transferred to a sucrose solution (30% in 0.1 M PBS with 0.02% sodium azide) for sectioning on a freezing microtome (American Optical Corp.). Forty micrometers of coronal sections were collected and stored in 12- or 24-well plates with sodium azide (0.02% in 0.1 M PBS). Spleens were stored in 0.1 M PBS with 0.02% sodium azide and sectioned on a vibratome (Leica T1000) at 50 μm; slices were stored in 12-well plates with 0.1 M PBS and 0.02% sodium azide. The TREM2 antibody required antigen retrieval, which involved incubating sections for 30 min at 75°C in 10 mM sodium citrate buffer (pH 6.0). Primary antibody concentration and incubation conditions were as follows: (i) rabbit anti-TMEM119: 1:1000 in 0.1 M PBS (RRID: AB_2800343); (ii) mouse anti–Iba1: 1:1000 in 0.1 M PBS (RRID: AB_10917271); (iii) rat anti-CD206: 1:1000 in 0.1 M PBS with 0.2% Triton X-100 and 2% bovine serum albumin (BSA; RRID: AB_322613); (iv) rat anti-CD68: 1:1000 in 0.1 M PBS with 0.2% Triton X-100 and 2% BSA (RRID: AB_324217); (v) rat anti-Gal3 (Mac2): 1:1000 in 0.1 M PBS with 0.2% Triton X-100 and 3% normal donkey serum (NDS; RRID: AB_10060357); and (vi) sheep anti-TREM2: 1:200 in 0.1 M PBS with 0.2% Triton X-100 and 5% NDS (RRID: AB_354956). All primary antibodies were incubated overnight at 4°C, with the exception of TREM2, which required a 2-day incubation at 4°C, and washed in 0.1 M PBS before incubation in secondary antibodies for 4 hours at room temperature (1:400 Cy5 donkey anti-rat, Invitrogen; 1:400 Cy5 goat anti-rabbit, Invitrogen; 1:500 Cy5 donkey anti-sheep and 1:500 Alexa Fluor 488 goat anti-mouse, Invitrogen; 1:400 Alexa Fluor 568 goat anti-rabbit, Invitrogen). Next, sections were incubated in Hoechst 33258 (1:1000 in 0.1 M PBS; Thermo Fisher Scientific) for 15 min and then washed and mounted on gelatin-coated glass slides and coverslipped with Fluoromount-G (SouthernBiotech).

Imaging of immunofluorescence-labeled sections was performed using an Olympus FV1000BX61W1 confocal microscope equipped with either a 20× objective (Olympus; NA = 0.75) or an oil-immersion 60× objective (Olympus; NA = 1.35). Images were collected using FV10-ASW software (RRID: SCR_014215) and the following settings for 20× or 60× image acquisition, respectively: zoom factor of ×1.8, 1024 by 1024 pixel resolution (0.345 μm per pixel), and 1 μm of *z*-step between subsequent slices or zoom factor of ×2.0, 1024 by 1024 pixel resolution (0.103 μm per pixel), and 0.75 μm of *z*-steps. Two images were averaged per plane in both imaging contexts.

Histological staining of blood cells

The depletion of circulating leukocytes following CLR treatment was quantified using a Diff-Quik staining kit (Electron Microscopy Sciences). A 1- to 3-μl drop of blood from the tail vein of a mouse was smeared on a glass slide and allowed to air-dry. Each animal provided five blood smears. Dry slides were dipped eight times, submerged for 1 s each time, in the following kit solutions: fixative (Fast Green in methanol), solution A (eosin G in phosphate buffer), and then solution B (thiazine dye in phosphate buffer). Excess solution was allowed to drain from the slide after each dip, and slides were rinsed in distilled water after solution B staining. Slides were air-dried and imaged with a bright-field microscope (Olympus BX-51) equipped with a 40× Olympus objective lens (NA = 0.65). Images were acquired in the monolayer of the blood smear, and 20 tiled images were taken per slide. Leukocytes were identified by morphological features: Neutrophils exhibited dark blue, multilobed nuclei, and pale pink cytoplasm; monocytes had dark purple nuclei and pale blue cytoplasm; and lymphocytes had dark blue nuclei surrounded by a barely distinguishable region of pale purple cytoplasm (see Fig. 3C). The RBCs counted in each imaging area were used to standardize the number of leukocytes quantified. The total number of leukocytes and RBCs counted per slide were averaged across the five slides obtained from each animal to comprise an individual sample.

Quantitative real-time polymerase chain reaction

RNA was extracted from flash-frozen brain tissue using an RNase Easy kit with deoxyribonuclease treatment following the manufacturer's instructions (QIAGEN, Canada). RNA concentrations were measured using NanoDrop 1000 (Thermo Fisher Scientific), and samples were stored at −80°C until further use. cDNA was synthesized from 100 ng of RNA and prepared using an high-capacity cDNA synthesis kit (Applied Biosystems) on a Bio-Rad T100 thermocycler (Bio-Rad, Mississauga, Ontario, Canada). cDNA was diluted fivefold for reverse transcription quantitative polymerase chain reaction (RT-qPCR) analysis. Primers were designed using the National Center for Biotechnology Information portal and OriGene, and primer amplification efficiencies and specificities were calculated using serial dilutions and melt curve analysis. RT-qPCR was carried out using 10 μl of reaction mixture (1 μl of cDNA, 2.5 pmol of each primer, and 5 μl of the SYBR Select Master Mix). Fluorescent signals were acquired by StepOnePlus RT-PCR System (Applied Biosystems), and data were analyzed using Design and Analysis software version 2.4.3 (Applied Biosystems). Thermocycling conditions used were 50°C (2 min), 95°C (2 min), followed by 40 cycles of 95°C denaturation (15 s), and 60°/62°C annealing (1 min). Triplicate reactions were performed for each sample, and C_t values were averaged and normalized to the expression of geometric mean of *Tbp* and *Hprt* using comparative C_t method ($\Delta\Delta C_t$) to calculate relative mRNA levels. The forward and reverse primers used for qPCR were as follows: *Lgals3* (*Gal3*), CCCAACGCAAACAGGATTGT and TGGTCAGCTTCAACCAGGAC; *Cd68*, ACTTCGGGCCATGTTTCTCTT and GGGGCTGGTAGGTTGATTGT; *Trem2*, CTTGCTGGAACCGTCACCAT and CTTGATTCCTGGAGGTGCTGT; *Tmem119*, CTTCACCCAGAGCTGGTTCCATA and CCGGGAGTGACACAGAGTAG; *Cd206* (*Mrc1*), ATCATTCCCTCAGCAAGCGA and GTGGATACTTGCCAGGTCCC; *TGFβ1*, TGATACGCCTGAGTGGCTGTCT and CACAAGAGCAGTGAGCGCTGAA; *TGFβR1*, TGCTCCAAACCACAGAGTAGGC and CCCAGAACACTAAGCCCATTGC; *Mertk*, TTGGGACGTTGGTGGATACG and CTTCTCGGCAGTGCCTCC; *Axl*, GACAACCCGGCCCTGC and CCTCGGTCTGTGTGTCCTTA; *Apoe*, GAACCGCTTCTGGGATTACCTG and GCCTTTACTTCCGTCATAGTGTC; *Tbp* (*housekeeping*), CCCCACAACTCTTCCATTCT and GCAGGAGTGATAGGGGTCAT; *Hprt* (*housekeeping*), AGCCTAAGATGAGCGCAAGT and TTACTAGGCAGATGGCCACA.

Analysis of microvascular blood flow velocity, diameter, length, and elimination

Blood flow velocity was quantified from line scans captured along the length of the microvessel, taken 30 to 60 s apart. Velocity was calculated on the basis of the inverse slope of the linear RBC streaks in the line scan. A minimum of three slopes per line scan, averaged across three line scans, were used to calculate the blood flow velocity. Microvessel diameter was determined as the full width at half maximum pixel gray values of a line's profile plotted perpendicular to the vessel. The length of a microvessel was also assessed as the distance, in three dimensions, between its nearest branch points. A microvessel was deemed eliminated if one end of the vessel had retracted completely from its original branch point and it lacked RBC streaking in line scans.

Analysis of microglia and macrophage responses to CMBs in vivo

To calculate the two-dimensional area of GFP-expressing cells around the CMB at each time point, the central plane of the *z*-stack was separated into red and green channels, and the resulting images were smoothed using a Gaussian filter (radius = 2.00). The images were binarized using a Li threshold, and the vessel region of interest (ROI) was selected in the red channel and overlaid on the green channel. The total area of signal pixels, corresponding to GFP-expressing cells, directly apposed to the overlaid selection was determined and constituted the two-dimensional area of GFP associated with the vessel. The percentage of vessel coverage was calculated using similarly processed images but involved tracing the left and right luminal aspects of the vessel in the binarized red channel. The total number of signal pixels intersecting with the two lines drawn across the vessel was expressed as a ratio of total pixels and determined the percent of vessel coverage by GFP-expressing cells. To determine the colocalization of lipofuscin autofluorescence with GFP, red and green channels were split for each plane in the acquired *z*-stack. Each image was smoothed using a Gaussian filter (radius = 1.00) and binarized using a Li threshold. ROIs were selected in the green channel and overlaid on the binarized red channel, and the percent colocalization was determined by dividing the total area of the ROIs by the total area of lipofuscin signal particles

encompassed by the ROIs over all planes in the *z*-stack. For experiments colocalizing lipofuscin with CD68 immunofluorescence, images of CD68, immunolabeled with Cy5, were acquired with the two-photon microscope at 900 nm, and lipofuscin particles were imaged at 750 nm. Signal from each substrate was overlaid to assess colocalization and expressed as a percentage.

Postmortem imaging and analysis of brain sections

CMBs induced in vivo, 3 days before collection of brain tissue, were identified in superficial layers of the right somatosensory cortex in postmortem brain sections. To assess the colocalization of Gal3 and TMEM119, single planes from confocal image stacks were split into individual channels. Images representing Gal3 and TMEM119 immunofluorescence were smoothed using a Gaussian filter (radius = 1.00) and binarized using a Li threshold. ROIs were selected from the channel representing TMEM119 immunostaining and overlaid on the channel representing Gal3. The area of the ROIs occupied by Gal3 signal pixels was determined for each plane in the stack, and the percent colocalization was calculated by dividing the total area of the ROIs by the total area of encapsulated pixels representing Gal3 immunostaining. Percent area of colocalization of CD68 with GFP and TREM2 with Iba1 was achieved using the same methods.

Morphological analyses of microglial soma cross-sectional area and total process length per cell were performed using Fiji software (RRID: SCR_002285). Briefly, 10 images from the center of two-photon image stacks (144 μm by 144 μm collected at 1.5 μm of *z*-step intervals), acquired before the induction of microbleeds, were *z*-projected (maximum intensity) and median-filtered. For soma quantification, a moments threshold was applied, and labeled soma were counted using the built-in analyze particles function. To estimate microglial process length, a Li threshold was applied to images, and resultant binary signals were dilated and then skeletonized. Total process length was estimated with the analyze particles function.

Recombinant AAV-BR1-Cre vector for labeling vascular endothelial cells

AAV-BR1-Cre vector was produced in Sf9 insect cells by the modified baculovirus expression system. Sf9 insect cells in Insect-XPRESS medium (Lonza, Basel, Switzerland) containing gentamycin (10 mg/liter) (Sigma-Aldrich, Darmstadt, Germany) was infected with high-titer stocks of two recombinant baculoviruses, one containing the AAV2-NRGTEWD ("AAV-BR1") rep and cap genes (*38*) and the other containing a CAG promoter–driven iCre expression cassette embedded between AAV2 inverted terminal repeats based on the pAAV-CAG-iCre plasmid. Cells were cultured in normal atmosphere at 27°C and 110 rpm. AAV-BR1-iCre vector was purified by ultracentrifugation in a discontinuous iodixanol gradient, according to a previously published protocol. After ultracentrifugation, the purified AAVs contained in the 40% iodixanol fraction were aspirated and transferred to 10,000 molecular weight cutoff Vivaspin tubes (Sartorius, Göttingen, Germany) for dialysis in PBS. To induce fluorescent labeling of vascular endothelial cells, td-tomato reporter mice (RRID: IMSR_JAX:007909) were intravenously injected with 25 μl of AAV-BR1-iCre, and their brains were collected 3 to 4 weeks later and prepared for immunohistochemistry.

Statistics

All imaging data were stored on a computer for off-line image processing with ImageJ (V1.52p, RRID:SCR_003070) and statistical analysis using GraphPad Prism (versions 7 and 8, RRID:SCR_002798). Two-tailed Student's *t* tests (paired or unpaired, as appropriate) were used to analyze differences between two groups. One-way ANOVAs were performed to compare differences between groups when a priori comparisons were not made. Two-way mixed-effects model ANOVAs were used to assess group differences over time. Significant main effects from ANOVAs were analyzed post hoc with Tukey's multiple comparisons tests. Chi-squared analyses were used for binomial data to determine whether microvessel elimination rates differed between groups. $P < 0.05$ was accepted as statistically significant. All experimental values are presented as means ± SEM.

SUPPLEMENTARY MATERIALS

Supplementary material for this article is available at http://advances.sciencemag.org/cgi/content/full/7/34/eabg2712/DC1

View/request a protocol for this paper from *Bio-protocol*.

REFERENCES AND NOTES

1. M. Merlini, V. A. Rafalski, P. E. Rios Coronado, T. M. Gill, M. Ellisman, G. Muthukumar, K. S. Subramanian, J. K. Ryu, C. A. Syme, D. Davalos, W. W. Seeley, L. Mucke, R. B. Nelson, K. Akassoglou, Fibrinogen induces microglia-mediated spine elimination and cognitive impairment in an Alzheimer's disease model. *Neuron* **101**, 1099–1108.e6 (2019).
2. N. L. Rosidi, J. Zhou, S. Pattanaik, P. Wang, W. Jin, M. Brophy, W. L. Olbricht, N. Nishimura, C. B. Schaffer, Cortical microhemorrhages cause local inflammation but do not trigger widespread dendrite degeneration. *PLOS ONE* **6**, e26612 (2011).
3. P. Reeson, K. A. Tennant, K. Gerrow, J. Wang, S. W. Novak, K. Thompson, K.-L. L. Lockhart, A. Holmes, P. C. Nahirney, C. E. Brown, Delayed inhibition of VEGF signaling after stroke attenuates blood–brain barrier breakdown and improves functional recovery in a comorbidity-dependent manner. *J. Neurosci.* **35**, 5128–5143 (2015).
4. C. Qiu, M. F. Cotch, S. Sigurdsson, P. V. Jonsson, M. K. Jonsdottir, S. Sveinbjrnsdottir, G. Eiriksdottir, R. Klein, T. B. Harris, M. A. van Buchem, V. Gudnason, L. J. Launer, Cerebral microbleeds, retinopathy, and dementia: The AGES-Reykjavik study. *Neurology* **75**, 2221–2228 (2010).
5. S. Akoudad, F. J. Wolters, A. Viswanathan, R. F. de Bruijn, A. van der Lugt, A. Hofman, P. J. Koudstaal, M. A. Ikram, M. W. Vernooij, Association of cerebral microbleeds with cognitive decline and dementia. *JAMA Neurol.* **73**, 934–943 (2016).
6. J. Woerdeman, E. van Duinkerken, M. P. Wattjes, F. Barkhof, F. J. Snoek, A. C. Moll, M. Klein, M. P. de Boer, R. G. Ijzerman, E. H. Serné, M. Diamant, Proliferative retinopathy in type 1 diabetes is associated with cerebral microbleeds, which is part of generalized microangiopathy. *Diabetes Care* **37**, 1165–1168 (2014).
7. C. Cordonnier, R. Al-Shahi Salman, J. Wardlaw, Spontaneous brain microbleeds: Systematic review, subgroup analyses and standards for study design and reporting. *Brain* **130**, 1988–2003 (2007).
8. S. Taylor, E. Mehina, E. White, P. Reeson, K. Yongblah, K. P. Doyle, C. E. Brown, Suppressing interferon-γ stimulates microglial responses and repair of microbleeds in the diabetic brain. *J. Neurosci.* **38**, 8707–8722 (2018).
9. F. Ginhoux, M. Greter, M. Leboeuf, S. Nandi, P. See, S. Gokhan, M. F. Mehler, S. J. Conway, L. G. Ng, E. R. Stanley, I. M. Samokhvalov, M. Merad, Fate mapping analysis reveals that adult microglia derive from primitive macrophages. *Science* **330**, 841–845 (2010).
10. M. Colonna, O. Butovsky, Microglia function in the central nervous system during health and neurodegeneration. *Annu. Rev. Immunol.* **35**, 441–468 (2017).
11. N. Lou, T. Takano, Y. Pei, A. L. Xavier, S. A. Goldman, M. Nedergaard, Purinergic receptor P2RY12-dependent microglial closure of the injured blood-brain barrier. *Proc. Natl. Acad. Sci. U.S.A.* **113**, 1074–1079 (2016).
12. S. J. Ahn, J. Anrather, N. Nishimura, C. B. Schaffer, Diverse inflammatory response after cerebral microbleeds includes coordinated microglial migration and proliferation. *Stroke* **49**, 1719–1726 (2018).
13. C. Zhang, N. R. Brandon, K. Koper, P. Tang, Y. Xu, H. Dou, Invasion of peripheral immune cells into brain parenchyma after cardiac arrest and resuscitation. *Aging Dis.* **9**, 412–425 (2018).
14. J. Herz, A. J. Filiano, A. Smith, N. Yogev, J. Kipnis, Myeloid cells in the central nervous system. *Immunity* **46**, 943–956 (2017).
15. C. Liu, C. Wu, Q. Yang, J. Gao, L. Li, D. Yang, L. Luo, Macrophages mediate the repair of brain vascular rupture through direct physical adhesion and mechanical traction. *Immunity* **44**, 1162–1176 (2016).
16. F. Binet, G. Mawambo, N. Sitaras, N. Tetreault, E. Lapalme, S. Favret, A. Cerani, D. Leboeuf, S. Tremblay, F. Rezende, A. M. Juan, A. Stahl, J. S. Joyal, É. Milot, R. J. Kaufman, M. Guimond, T. E. Kennedy, P. Sapieha, Neuronal ER stress impedes myeloid-cell-induced

vascular regeneration through IRE1α degradation of netrin-1. *Cell Metab.* **17**, 353–371 (2013).
17. D. A. Galloway, A. E. M. Phillips, D. R. J. Owen, C. S. Moore, Phagocytosis in the brain: Homeostasis and disease. *Front. Immunol.* **10**, 790 (2019).
18. A. D. Greenhalgh, S. David, Differences in the phagocytic response of microglia and peripheral macrophages after spinal cord injury and its effects on cell death. *J. Neurosci.* **34**, 6316–6322 (2014).
19. S. K. Halder, R. Milner, A critical role for microglia in maintaining vascular integrity in the hypoxic spinal cord. *Proc. Natl. Acad. Sci. U.S.A.* **116**, 26029–26037 (2019).
20. C. Condello, P. Yuan, A. Schain, J. Grutzendler, Microglia constitute a barrier that prevents neurotoxic protofibrillar Aβ42 hotspots around plaques. *Nat. Commun.* **6**, 6176 (2015).
21. V. Jolivel, F. Bicker, F. Binamé, R. Ploen, S. Keller, R. Gollan, B. Jurek, J. Birkenstock, L. Poisa-Beiro, J. Bruttger, V. Opitz, S. C. Thal, A. Waisman, T. Bäuerle, M. K. Schäfer, F. Zipp, M. H. H. Schmidt, Perivascular microglia promote blood vessel disintegration in the ischemic penumbra. *Acta Neuropathol.* **129**, 279–295 (2015).
22. U. C. Schneider, A. M. Davids, S. Brandenburg, A. Müller, A. Elke, S. Magrini, E. Atangana, K. Turkowski, T. Finger, A. Gutenberg, C. Gehlhaar, W. Brück, F. L. Heppner, P. Vajkoczy, Microglia inflict delayed brain injury after subarachnoid hemorrhage. *Acta Neuropathol.* **130**, 215–231 (2015).
23. D. Davalos, J. Kyu Ryu, M. Merlini, K. M. Baeten, N. Le Moan, M. A. Petersen, T. J. Deerinck, D. S. Smirnoff, C. Bedard, H. Hakozaki, S. Gonias Murray, J. B. Ling, H. Lassmann, J. L. Degen, M. H. Ellisman, K. Akassoglou, Fibrinogen-induced perivascular microglial clustering is required for the development of axonal damage in neuroinflammation. *Nat. Commun.* **3**, 1227 (2012).
24. M. Fuhrmann, T. Bittner, C. K. E. Jung, S. Burgold, R. M. Page, G. Mitteregger, C. Haass, F. M. Laferla, H. Kretzschmar, J. Herms, Microglial Cx3cr1 knockout prevents neuron loss in a mouse model of Alzheimer's disease. *Nat. Neurosci.* **13**, 411–413 (2010).
25. S. Krasemann, C. Madore, R. Cialic, C. Baufeld, N. Calcagno, R. El Fatimy, L. Beckers, E. O'Loughlin, Y. Xu, Z. Fanek, D. J. Greco, S. T. Smith, G. Tweet, Z. Humulock, T. Zrzavy, P. Conde-Sanroman, M. Gacias, Z. Weng, H. Chen, E. Tjon, F. Mazaheri, K. Hartmann, A. Madi, J. D. Ulrich, M. Glatzel, A. Worthmann, J. Heeren, B. Budnik, C. Lemere, T. Ikezu, F. L. Heppner, V. Litvak, D. M. Holtzman, H. Lassmann, H. L. Weiner, J. Ochando, C. Haass, O. Butovsky, The TREM2-APOE pathway drives the transcriptional phenotype of dysfunctional microglia in neurodegenerative diseases. *Immunity* **47**, 566–581.e9 (2017).
26. T. R. Hammond, C. Dufort, L. Dissing-Olesen, S. Giera, A. Young, A. Wysoker, A. J. Walker, F. Gergits, M. Segel, J. Nemesh, S. E. Marsh, A. Saunders, E. Macosko, F. Ginhoux, J. Chen, R. J. M. Franklin, X. Piao, S. A. McCarroll, B. Stevens, Single-cell RNA sequencing of microglia throughout the mouse lifespan and in the injured brain reveals complex cell-state changes. *Immunity* **50**, 253–271.e6 (2019).
27. A. Nimmerjahn, F. Kirchhoff, F. Helmchen, Resting microglial cells are highly dynamic surveillants of brain parenchyma in vivo. *Science* **308**, 1314–1318 (2005).
28. M. L. Bennett, F. C. Bennett, S. A. Liddelow, B. Ajami, J. L. Zamanian, N. B. Fernhoff, S. B. Mulinyawe, C. J. Bohlen, A. Adil, A. Tucker, I. L. Weissman, E. F. Chang, G. Li, G. A. Grant, M. G. Hayden Gephart, B. A. Barres, New tools for studying microglia in the mouse and human CNS. *Proc. Natl. Acad. Sci. U.S.A.* **113**, E1738–E1746 (2016).
29. R. Ward, J. Paul Valenzuela, W. Li, G. Dong, S. C. Fagan, A. Ergul, Poststroke cognitive impairment and hippocampal neurovascular remodeling: The impact of diabetes and sex. *Am. J. Physiol. Hear. Circ. Physiol.* **315**, H1402–H1413 (2018).
30. B. Vuong, G. Odero, S. Rozbacher, M. Stevenson, S. M. Kereliuk, T. J. Pereira, V. W. Dolinsky, T. M. Kauppinen, Exposure to gestational diabetes mellitus induces neuroinflammation, derangement of hippocampal neurons, and cognitive changes in rat offspring. *J. Neuroinflammation* **14**, 80 (2017).
31. M. R. P. Elmore, A. R. Najafi, M. A. Koike, N. N. Dagher, E. E. Spangenberg, R. A. Rice, M. Kitazawa, B. Matusow, H. Nguyen, B. L. West, K. N. Green, Colony-stimulating factor 1 receptor signaling is necessary for microglia viability, unmasking a microglia progenitor cell in the adult brain. *Neuron* **82**, 380–397 (2014).
32. J. R. Plemel, J. A. Stratton, N. J. Michaels, K. S. Rawji, E. Zhang, S. Sinha, C. S. Baaklini, Y. Dong, M. Ho, K. Thorburn, T. N. Friedman, S. Jawad, C. Silva, A. V. Caprariello, V. Hoghooghi, J. Yue, A. Jaffer, K. Lee, B. J. Kerr, R. Midha, P. K. Stys, J. Biernaskie, V. W. Yong, V. Wee Yong, Microglia response following acute demyelination is heterogeneous and limits infiltrating macrophage dispersion. *Sci. Adv.* **6**, eaay6324 (2020).
33. J. C. Cronk, A. J. Filiano, A. Louveau, I. Marin, R. Marsh, E. Ji, D. H. Goldman, I. Smirnov, N. Geraci, S. Acton, C. C. Overall, J. Kipnis, Peripherally derived macrophages can engraft the brain independent of irradiation and maintain an identity distinct from microglia. *J. Exp. Med.* **215**, 1627–1647 (2018).
34. G. Faraco, Y. Sugiyama, D. Lane, L. Garcia-Bonilla, H. Chang, M. M. Santisteban, G. Racchumi, M. Murphy, N. Van Rooijen, J. Anrather, C. Iadecola, Perivascular macrophages mediate the neurovascular and cognitive dysfunction associated with hypertension. *J. Clin. Invest.* **126**, 4674–4689 (2016).
35. L. Zhan, L. Fan, L. Kodama, P. D. Sohn, M. Y. Wong, G. A. Mousa, Y. Zhou, Y. Li, L. Gan, A MAC2-positive progenitor-like microglial population is resistant to CSF1R inhibition in adult mouse brain. *eLife* **9**, e51796 (2020).
36. F. N. Ziyadeh, K. Sharma, M. Ericksen, G. Wolf, Stimulation of collagen gene expression and protein synthesis in murine mesangial cells by high glucose is mediated by autocrine activation of transforming growth factor-beta. *J. Clin. Invest.* **93**, 536–542 (1994).
37. T. Masuda, L. Amann, R. Sankowski, O. Staszewski, M. Lenz, P. d'Errico, N. Snaidero, M. J. Costa Jordão, C. Böttcher, K. Kierdorf, S. Jung, J. Priller, T. Misgeld, A. Vlachos, M. M. Luehmann, K.-P. Knobeloch, M. Prinz, Novel Hexb-based tools for studying microglia in the CNS. *Nat. Immunol.* **21**, 802–815 (2020).
38. J. Körbelin, G. Dogbevia, S. Michelfelder, D. A. Ridder, A. Hunger, J. Wenzel, H. Seismann, M. Lampe, J. Bannach, M. Pasparakis, J. A. Kleinschmidt, M. Schwaninger, M. Trepel, A brain microvasculature endothelial cell-specific viral vector with the potential to treat neurovascular and neurological diseases. *EMBO Mol. Med.* **8**, 609–625 (2016).
39. M. J. Abedin, Y. Kashio, M. Seki, K. Nakamura, M. Hirashima, Potential roles of galectins in myeloid differentiation into three different lineages. *J. Leukoc. Biol.* **73**, 650–656 (2003).
40. M. M. J. Polfliet, P. H. Goede, E. M. L. Van Kesteren-Hendrikx, N. Van Rooijen, C. D. Dijkstra, T. K. Van den Berg, A method for the selective depletion of perivascular and meningeal macrophages in the central nervous system. *J. Neuroimmunol.* **116**, 188–195 (2001).
41. P. Yuan, C. Condello, C. D. Keene, Y. Wang, T. D. Bird, S. M. Paul, W. Luo, M. Colonna, D. Baddeley, J. Grutzendler, TREM2 haplodeficiency in mice and humans impairs the microglia barrier function leading to decreased amyloid compaction and severe axonal dystrophy. *Neuron* **90**, 724–739 (2016).
42. B. Ajami, N. Samusik, P. Wieghofer, P. P. Ho, A. Crotti, Z. Bjornson, M. Prinz, W. J. Fantl, G. P. Nolan, L. Steinman, Single-cell mass cytometry reveals distinct populations of brain myeloid cells in mouse neuroinflammation and neurodegeneration models. *Nat. Neurosci.* **21**, 541–551 (2018).
43. M. Prinz, J. Priller, The role of peripheral immune cells in the CNS in steady state and disease. *Nat. Neurosci.* **20**, 136–144 (2017).
44. A. Deczkowska, H. Keren-Shaul, A. Weiner, M. Colonna, M. Schwartz, I. Amit, Disease-associated microglia: A universal immune sensor of neurodegeneration. *Cell* **173**, 1073–1081 (2018).
45. R. Rahimian, L. C. Béland, J. Kriz, Galectin-3: Mediator of microglia responses in injured brain. *Drug Discov. Today* **23**, 375–381 (2018).
46. L. J. Trigiani, M. Lacalle-Aurioles, M. Bourourou, L. Li, A. D. Greenhalgh, J. G. Zarruk, S. David, M. G. Fehlings, E. Hamel, Benefits of physical exercise on cognition and glial white matter pathology in a mouse model of vascular cognitive impairment and dementia. *Glia* **68**, 1925–1940 (2020).
47. M. Lalancette-Hébert, V. Swarup, J. M. Beaulieu, I. Bohacek, E. Abdelhamid, Y. C. Weng, S. Sato, J. Kriz, Galectin-3 is required for resident microglia activation and proliferation in response to ischemic injury. *J. Neurosci.* **32**, 10383–10395 (2012).
48. M. Lalancette-Hébert, G. Gowing, A. Simard, C. W. Yuan, J. Kriz, Selective ablation of proliferating microglial cells exacerbates ischemic injury in the brain. *J. Neurosci.* **27**, 2596–2605 (2007).
49. G. Pugliese, F. Pricci, C. Iacobini, G. Leto, L. Amadio, P. Barsotti, L. Frigeri, D. K. Hsu, H. Vlassara, F.-T. Liu, U. Di Mario, Accelerated diabetic glomerulopathy in galectin-3/AGE receptor 3 knockout mice. *FASEB J.* **15**, 2471–2479 (2001).
50. J. J. Siew, H.-M. Chen, H.-Y. Chen, H.-L. Chen, C.-M. Chen, B.-W. Soong, Y.-R. Wu, C.-P. Chang, Y.-C. Chan, C.-H. Lin, F.-T. Liu, Y. Chern, Galectin-3 is required for the microglia-mediated brain inflammation in a model of Huntington's disease. *Nat. Commun.* **10**, 3473 (2019).
51. C. Venkatesan, M. A. Chrzaszcz, N. Choi, M. S. Wainwright, Chronic upregulation of activated microglia immunoreactive for galectin-3/Mac-2 and nerve growth factor following diffuse axonal injury. *J. Neuroinflammation* **7**, 32 (2010).
52. M. A. Burguillos, M. Svensson, T. Schulte, A. Boza-Serrano, A. Garcia-Quintanilla, E. Kavanagh, M. Santiago, N. Viceconte, M. J. Oliva-Martin, A. M. Osman, E. Salomonsson, L. Amar, A. Persson, K. Blomgren, A. Achour, E. Englund, H. Leffler, J. L. Venero, B. Joseph, T. Deierborg, Microglia-secreted galectin-3 acts as a Toll-like receptor 4 ligand and contributes to microglial activation. *Cell Rep.* **10**, 1626–1638 (2015).
53. J. Nieminen, A. Kuno, J. Hirabayashi, S. Sato, Visualization of galectin-3 oligomerization on the surface of neutrophils and endothelial cells using fluorescence resonance energy transfer. *J. Biol. Chem.* **282**, 1374–1383 (2007).
54. L. Díaz-Alvarez, E. Ortega, The many roles of galectin-3, a multifaceted molecule, in innate immune responses against pathogens. *Mediators Inflamm.* **2017**, 9247574 (2017).
55. Y. Okuda, Y. Nakatsuji, H. Fujimura, H. Esumi, T. Ogura, T. Yanagihara, S. Sakoda, Expression of the inducible isoform of nitric oxide synthase in the central nervous system of mice correlates with the severity of actively induced experimental allergic encephalomyelitis. *J. Neuroimmunol.* **62**, 103–112 (1995).
56. A. Mishra, E. A. Newman, Inhibition of inducible nitric oxide synthase reverses the loss of functional hyperemia in diabetic retinopathy. *Glia* **58**, 1996–2004 (2010).

57. A. Boza-Serrano, R. Ruiz, R. Sanchez-Varo, J. García-Revilla, Y. Yang, I. Jimenez-Ferrer, A. Paulus, M. Wennström, A. Vilalta, D. Allendorf, J. C. Davila, J. Stegmayr, S. Jiménez, M. A. Roca-Ceballos, V. Navarro-Garrido, M. Swanberg, C. L. Hsieh, L. M. Real, E. Englund, S. Linse, H. Leffler, U. J. Nilsson, G. C. Brown, A. Gutierrez, J. Vitorica, J. L. Venero, T. Deierborg, Galectin-3, a novel endogenous TREM2 ligand, detrimentally regulates inflammatory response in Alzheimer's disease. *Acta Neuropathol.* **138**, 251–273 (2019).
58. H.-R. Chen, Y.-Y. Sun, C.-W. Chen, Y.-M. Kuo, I. S. Kuan, Z.-R. Tiger Li, J. C. Short-Miller, M. R. Smucker, C.-Y. Kuan, Fate mapping via CCR2-CreER mice reveals monocyte-to-microglia transition in development and neonatal stroke. *Sci. Adv.* **6**, eabb2119 (2020).
59. M. Gelderblom, F. Leypoldt, K. Steinbach, D. Behrens, C. U. Choe, D. A. Siler, T. V. Arumugam, E. Orthey, C. Gerloff, E. Tolosa, T. Magnus, Temporal and spatial dynamics of cerebral immune cell accumulation in stroke. *Stroke* **40**, 1849–1857 (2009).
60. L. Quagliaro, L. Piconi, R. Assaloni, R. Da Ros, A. Maier, G. Zuodar, A. Ceriello, Intermittent high glucose enhances ICAM-1, VCAM-1 and E-selectin expression in human umbilical vein endothelial cells in culture: The distinct role of protein kinase C and mitochondrial superoxide production. *Atherosclerosis* **183**, 259–267 (2005).
61. E. Kim, J. Yang, K. W. Park, S. Cho, Inhibition of VEGF signaling reduces diabetes-exacerbated brain swelling, but not infarct size, in large cerebral infarction in mice. *Transl. Stroke Res.* **9**, 540–548 (2018).
62. F. Herisson, V. Frodermann, G. Courties, D. Rohde, Y. Sun, K. Vandoorne, G. R. Wojtkiewicz, G. S. Masson, C. Vinegoni, J. Kim, D. E. Kim, R. Weissleder, F. K. Swirski, M. A. Moskowitz, M. Nahrendorf, Direct vascular channels connect skull bone marrow and the brain surface enabling myeloid cell migration. *Nat. Neurosci.* **21**, 1209–1217 (2018).
63. T. L. Roth, D. Nayak, T. Atanasijevic, A. P. Koretsky, L. L. Latour, D. B. McGavern, Transcranial amelioration of inflammation and cell death after brain injury. *Nature* **505**, 223–228 (2014).
64. A. Mildner, B. Schlevogt, K. Kierdorf, C. Böttcher, D. Erny, M. P. Kummer, M. Quinn, W. Brück, I. Bechmann, M. T. Heneka, J. Priller, M. Prinz, Distinct and non-redundant roles of microglia and myeloid subsets in mouse models of Alzheimer's disease. *J. Neurosci.* **31**, 11159–11171 (2011).
65. B. Ajami, J. L. Bennett, C. Krieger, K. M. McNagny, F. M. V. Rossi, Infiltrating monocytes trigger EAE progression, but do not contribute to the resident microglia pool. *Nat. Neurosci.* **14**, 1142–1149 (2011).
66. A. Paré, B. Mailhot, S. A. Lévesque, C. Juzwik, P. M. I. A. Doss, M.-A. Lécuyer, A. Prat, M. Rangachari, A. Fournier, S. Lacroix, IL-1β enables CNS access to $CCR2^{hi}$ monocytes and the generation of pathogenic cells through GM-CSF released by CNS endothelial cells. *Proc. Natl. Acad. Sci. U.S.A.* **115**, E1194–E1203 (2018).
67. R. Cayrol, K. Wosik, J. L. Berard, A. Dodelet-Devillers, I. Ifergan, H. Kebir, A. S. Haqqani, K. Kreymborg, S. Krug, R. Moumdjian, A. Bouthillier, B. Becher, N. Arbour, S. David, D. Stanimirovic, A. Prat, Activated leukocyte cell adhesion molecule promotes leukocyte trafficking into the central nervous system. *Nat. Immunol.* **9**, 137–145 (2008).
68. A. D. Greenhalgh, J. G. Zarruk, L. M. Healy, S. J. Baskar Jesudasan, P. Jhelum, C. K. Salmon, A. Formanek, M. V. Russo, J. P. Antel, D. B. McGavern, B. W. McColl, S. David, Peripherally derived macrophages modulate microglial function to reduce inflammation after CNS injury. *PLOS Biol.* **16**, e2005264 (2018).
69. M. S. Unger, P. Schernthaner, J. Marschallinger, H. Mrowetz, L. Aigner, Microglia prevent peripheral immune cell invasion and promote an anti-inflammatory environment in the brain of APP-PS1 transgenic mice. *J. Neuroinflammation* **15**, 274 (2018).
70. G. J. Biessels, I. J. Deary, C. M. Ryan, Cognition and diabetes: A lifespan perspective. *Lancet Neurol.* **7**, 184–190 (2008).
71. E. Van Duinkerken, M. M. Schoonheim, E. J. Sanz-Arigita, R. G. IJzerman, A. C. Moll, F. J. Snoek, C. M. Ryan, M. Klein, M. Diamant, F. Barkhof, Resting-state brain networks in type 1 diabetic patients with and without microangiopathy and their relation to cognitive functions and disease variables. *Diabetes* **61**, 1814–1821 (2012).
72. S. Jung, J. Aliberti, P. Graemmel, M. J. Sunshine, G. W. Kreutzberg, A. Sher, D. R. Littman, Analysis of fractalkine receptor CX_3CR1 function by targeted deletion and green fluorescent protein reporter gene insertion. *Mol. Cell. Biol.* **20**, 4106–4114 (2000).

Acknowledgments: We would like to thank M.-E. Tremblay, L. A. Swayne, and B. Chow for advice and comments on the manuscript, as well as T. Yang and the ACU staff for animal colony husbandry and management. **Funding:** This work was supported by operating, salary, and equipment grants to C.E.B. from the Canadian Institutes of Health Research (CIHR), Heart and Stroke Foundation (HSF), Natural Sciences and Engineering Research Council of Canada (NSERC), and Canadian Foundation for Innovation (CFI). E.M.F.M. was supported by an NSERC Vanier CGS-D scholarship. **Author contributions:** E.M.F.M. and C.E.B. conceived the study and co-wrote the manuscript. E.M.F.M. and C.E.B. supervised the project. E.M.F.M., S.T., R.B., E.W., S.E.C., M.S.C., and C.E.B. performed experiments and collected data; E.M.F.M., S.T., R.B., S.E.C., M.S.C., and C.E.B. analyzed data. J.K. provided valuable reagents. All authors discussed the results and commented on the manuscript. **Competing interests:** J.K. is an inventor on a patent related to this work filed by Boehringer Ingelheim International GmbH (no. US10287318B2, published 14 May 2019). The authors declare that they have no other competing interests. **Data and materials availability:** All data needed to evaluate the conclusions in the paper are present in the paper and/or the Supplementary Materials. The AAV-BR1-Cre vector can be provided by J.K. pending scientific review and a completed material transfer agreement. Requests for the AAV-BR1-Cre vector should be submitted to J.K. (j.koerbelin@uke.de).

Submitted 21 December 2020
Accepted 28 June 2021
Published 18 August 2021
10.1126/sciadv.abg2712

Citation: E. M. F. Mehina, S. Taylor, R. Boghozian, E. White, S. E. Choi, M. S. Cheema, J. Korbelin, C. E. Brown, Invasion of phagocytic Galectin 3 expressing macrophages in the diabetic brain disrupts vascular repair. *Sci. Adv.* **7**, eabg2712 (2021).